Journal of Wind Engineering & Industrial Aerodynamics 265 (2025) 106174

Contents lists available at ScienceDirect

Journal of Wind Engineering & Industrial Aerodynamics

journal homepage: www.elsevier.com/locate/jweia

Effects of façade and rooftop greening on the surface pressure distribution of an isolated cubic building with side wall apertures

Vasiliki Pappa [a,*], Asterios Bakolas [b], Demetri Bouris [a], Christof Gromke [c]

[a] Laboratory for Innovative Environmental Technologies, School of Mechanical Engineering, National Technical University of Athens, 9 Iroon Polytechneiou str., 15773 Athens, Greece

[b] Department of Materials Science and Engineering, School of Chemical Engineering, National Technical University of Athens, 9 Iroon Polytechneiou str., 15773 Athens, Greece

[c] Laboratory of Building and Environmental Aerodynamics, Institute for Water and Environment, Karlsruhe Institute of Technology, Kaiserstrasse 12, 76128 Karlsruhe, Germany

ARTICLE INFO

Keywords:
Surface pressure measurements
Façade greening
Rooftop greening
Wind tunnel experiments
Power spectrum analysis

ABSTRACT

Greening is considered a sustainable and environmentally friendly policy for urban development but despite the progress made so far, the aerodynamic implications of building embedded greening have yet to be determined. Greening may have a variety of implications on wind loads, natural ventilation and air exchange, all related to the pressure distribution on buildings' external surfaces. In the present study, a wind tunnel investigation deals with the qualitative and quantitative effects of building greening on the external surface pressure distribution of a model building. Greening was considered to fully cover the external windward façade and the roof under various permeabilities and thicknesses. Openings on the side walls allow for indoor–outdoor air exchange. The position and the thickness of greening were found to be decisive parameters for the overall pressure distribution but attention was also directed towards the fluctuating pressures near the openings, which are expected to be the driving mechanism for air exchange in this configuration. Effects of rooftop greening were confined mainly to the roof and the wake but for windward façade greening, mean and fluctuating pressure differences of up to 35%, compared to the bare building, were observed in the vicinity of the openings. The major effect was a damping of the lower frequencies of pressure fluctuations and it had a stronger dependence on the thickness rather than the material properties of the windward façade greening.

1. Introduction

Modern cities incorporate many of humanity's technological achievements, including contemporary architecture, means of transport and communication, even energy production. The harmonious balance between these and the natural habitat is considered by many to be the key for cities that are inclusive, safe, resilient and sustainable (UN Cities, 2015). A crucial parameter of this harmonious coexistence in the urban environment is airing (Sandberg et al., 2020). Understanding airing through buildings and/or building openings on a large scale, as in the case of an entire city, or on a smaller local scale, in a neighbourhood or a single building, can be an effective way to address a wide range of issues and applications. It may be expected to improve natural ventilation and reduce energy consumption, compared to continuous mechanical ventilation (Hayati et al., 2019), to mitigate contaminant concentration peaks indoors (Sandberg et al., 2020) and to reduce peak wind loads (Ciarlatani et al., 2023), contributing to wind-resistant building design.

The connection between the mean and fluctuating pressure distribution on the external surfaces of a building and the air flow through its openings is well established (Etheridge and Sandberg, 1996; Haghighat et al., 2000), but the aim of the present study is to understand the effects on surface pressure distribution when different types of vegetation are installed on the building's outer surfaces. As green roofs and façade greening are part of Urban Green Infrastructure (UGI) and are widely used concepts for the urban built environment in both the Mediterranean and Central Europe, these two types of vegetation installations were selected for further investigation.

Vegetation is a complex living organism, both in terms of structure and functionality. For wind flow in particular, it is considered as a porous body comprising branches, stems and leaves (Gromke, 2011) while, at the same time it functions under five main mechanisms i.e. transpiration, shading, radiation trapping, pollutant deposition and aerodynamic effects (Li et al., 2022). However, previous research (Buccolieri et al., 2018) points out that the aerodynamic effects of

* Corresponding author.
E-mail address: vaspappa@mail.ntua.gr (V. Pappa).

https://doi.org/10.1016/j.jweia.2025.106174
Received 20 December 2024; Received in revised form 20 May 2025; Accepted 5 July 2025
Available online 23 July 2025

Nomenclature

Symbols

A	Surface
C	Form drag coefficient (m^{-1})
C_d	Drag coefficient of a vegetation element
d	Displacement thickness (m)
f	Frequency (Hz)
F_d	Drag force (N)
F_w	Momentum wind force (N)
h	Opening height (mm)
h_e	Roughness elements height (mm)
H	Building height (mm)
$I_u(z)$	Turbulence intensity at a given height, z (–)
K	Permeability (Darcy–Forchheimer) (m^2)
LAD	Leaf area density ($m^2\ m^{-3}$)
LAI	Leaf area index ($m^2\ m^{-2}$)
M	Scale factor
p	Pressure (Pa)
P	Pore fraction (%)
p_o	Static reference pressure (Pa)
$p(t)$	Time-series pressure signal (Pa)
Re	Reynolds number
Re_*	Minimum Reynolds number
S_{tr}	Strouhal number
t	Time (s)
T	Vegetation layer thickness (mm)
T_L	5 mm in reduced-scale, 1.5 m in full-scale, vegetation layer thickness
T_{2L}	10 mm in reduced-scale, 3.0 m in full-scale, vegetation layer thickness
U	Average streamwise wind velocity (m/s)
u_∞	Free stream velocity (m/s)
$u(z)$	Streamwise velocity at a given height, z (m/s)
w	Opening width (mm)
z_0	Roughness length (mm)

Greek

α	power law coefficient (–)
$\Delta\Theta$	Temperature variation (°C)
Δp	Pressure difference (Pa)
δp	Pressure error (Pa)
ΔP	Pressure drop (Pa)
ϵ	Porosity (%)
Θ	Temperature (°C)
κ	von Karman constant
λ	Pressure loss coefficient/permeability (m^{-1})
μ	Fluid medium viscosity (Pa s)
ρ	Fluid medium density ($kg\ m^{-3}$)

Acronyms

3D	Three-dimensional
ABL	Atmospheric boundary layer
CTA	Constant temperature anemometry
DSF	Double-skin porous façade system
FSO	Full-Scale Output
IIR	Infinite Impulse Response
KIT	Karlsruhe Institute of Technology
LES	Large Eddy Simulations
NTUA	National Technical University of Athens
PPI	Pores per inch
RANS	Reynolds-Averaged Navier–Stokes
VDI	Verein Deutscher Ingenieure

Sub Scripts

ac	Acquisition
b	Branch
co	Cutting-off
Coverage	Coverage ratio of foam
cs	Cross-sectional
Dynamic	Dynamic
Fluct	Fluctuating
fs	Full scale
Greening	With greening
H	Model building height
Leeward	Leeward
mean	mean
Meas	Measurement
No greening	Without greening
rs	Reduced scale
ref	Reference point
rel	Relative differences between vegetation scenario and the reference scenario (without vegetation)
s	Sampling
Shedding	Vortex shedding
Static	Static
Tap	Tap
Vol	Volume
Windward	Windward

vegetation with regard to urban air quality can be stronger than the positive effects of pollutant deposition. Furthermore, according to Li et al. (2022), the aerodynamic impact of urban green infrastructure largely depends on the position of the vegetation, its properties and its geometric characteristics. Based on the above, aerodynamic effects and their relation to these three vegetation parameters were the main focus of the present investigation.

Wind tunnel studies focusing on vegetation effects can be divided into two main categories: studies where natural trees and/or shrubs are placed in the wind tunnel and their properties are measured, mainly the drag coefficient (Mayhead, 1973; Rudnicki et al., 2004; Vollsinger et al., 2005; Kane and Smiley, 2006; Cao et al., 2012; Manickathan et al., 2018) and secondly wind tunnel studies that artificially model real vegetation types and species. In one of the first studies belonging to the second group, vegetation was represented by injection-molded Nylon-66 stems with low-density polyethylene branch elements (Stacey et al., 1994) to meet aerodynamic and structural dynamic similarity criteria. In more recent studies, metal wire meshes (Aubrun and Leitl, 2004; Dellwik et al., 2023) or porous foams (Gromke, 2011; Gromke et al., 2016; Li et al., 2022; Pappa et al., 2023) have been used to characterize the aerodynamic behaviour of trees/vegetation in an abstract way. Other researchers have used miniature plastic trees (Manickathan et al., 2018; Fellini et al., 2022) to mimic natural trees and characterized their aerodynamic behaviour by evaluating their aerodynamic porosity and drag coefficient.

In order to focus on the aerodynamic effects of building embedded vegetation, this work takes a step back from the complex flow structures of an entire city or a part of it and considers an isolated cubic model building with openings, exposed to a simulated atmospheric boundary layer. The experimental setup of an isolated building without openings has been studied by many researchers over the years (Castro and Robins, 1977; Lim et al., 2007; Hearst et al., 2016; Papp et al., 2021), as has that of an isolated building with openings (Karava et al., 2011; Manolesos et al., 2018; Pappa et al., 2019; Jiang et al., 2022;

Biswas and Vanderwel, 2024). The fluid structures appearing on and around the building are well established i.e. stagnation point, separation zones, recirculation and reattachment regions (Cao et al., 2022). However, to the authors' knowledge, the interaction of vegetation with these flow structures has not yet been investigated. Furthermore, the result of this interaction on the building's outer wall pressure field is unknown. Does the vegetation affect the pressure field and thus the ventilation mechanism, if we intervene on the building face where the stagnation point exists i.e. on the windward façade wall and in the areas where critical points have been identified, including separation and recirculation points on the roof ? And if so, how much these pressure values change ? Based on the aforementioned research inquiries, we performed a wind tunnel study that deals with the qualitative and quantitative effects on the model building's external wall pressure when vegetation is placed on the external windward building façade or on the building roof. It is related to a recent study (Pappa et al., 2023) where the effects of façade and rooftop greening on the indoor air quality of the model building were investigated and air exchange rates were calculated indirectly through tracer gas concentration measurements. Here, the emphasis is on the pressure field around the model building, as pressure is the driving force for the air exchange rate through the building openings. However, it should be noted that the pressure field is also of interest for other applications, such as the prediction of local wind pressure loads. In the future, we intend to extend the concept of implanted vegetation to more complex terrains (i.e. urban street canyons) but before moving on a multi-parametric system, we must first evaluate its effects on the pressure field in a simpler urban environment.

The rest of this article is organized as follows. Section 2 consists of a detailed description of the atmospheric boundary layer simulation, the geometry of the model building, and the similarity considerations taken into account in the vegetation modelling. Section 3 describes the pressure measurement set-up, presents the test cases and explains the post-processing analysis of the pressure signal, including its uncertainties. Section 4 shows the results of the pressure measurements with and without vegetation, compares the effects of vegetation positioning and vegetation properties and demonstrates the results of the power spectrum analysis for the case with the most prominent effect in the vicinity of the openings, i.e. the windward façade greening. Section 5 summarizes the main conclusions of this work.

2. Wind tunnel experiments: Materials and simulations

2.1. Atmospheric boundary layer

The experiments were performed in an atmospheric boundary layer (ABL) wind tunnel at the Laboratory of Building and Environmental Aerodynamics at the Karlsruhe Institute of Technology (KIT) (Fig. 1a). The boundary layer wind tunnel has a cross section of 2 m by 1 m (width by height) with an adjustable ceiling to allow flow with vanishing pressure gradient in the streamwise direction ($dp/dx = 0$). The ABL simulation was created using Irwin-type vortex generators, a horizontally ground-mounted tripping device and a fetch of 6 m length covered with surface roughness elements.

The instantaneous streamwise velocity was measured at 29 points along a vertical line above the centre of the wind tunnel floor, without a model in the test section. A single hot wire sensor was used, operating in a constant temperature mode (Constant Temperature Anemometry, CTA). The velocity signal was sampled at 6 kHz for a total measurement time of 60 s. Three main flow characteristics were determined: the mean wind velocity profile $u(z)$, the turbulence intensity I_u and the integral length scale L_{ux} in the streamwise direction (Fig. 1b–d, respectively).

In order to assess and compare the simulated boundary layer characteristics with internationally accepted standards (VDI 3783, 2000; Eurocode, 2005), two equations are fitted to the experimental mean velocity dataset: the logarithmic law and the power law. The experimental results were fitted to the logarithmic law to determine the aerodynamic roughness length z_0 and the friction velocity u_* and to the power law to estimate the profile exponent α, which indicates the roughness of the terrain.

During the experimental procedure, the free stream velocity at the top of the boundary layer was set to $u_\infty = 5$ m/s. The height of the model building (see Section 2.2), i.e. $H = 110$ mm, was selected as the reference height, the displacement thickness d was set to zero, and the reference velocity u_H, was measured to be 3.27 m/s. The boundary layer height δ was 0.5 m. The critical Reynolds number for bluff bodies' flow insensitivity, based on Lim et al. (2007) should be between 2 - $3{\cdot}10^4$, while in Gromke (2018) a Re lower limit of $1.5 \cdot 10^4$ is suggested. Furthermore, according to Lim et al. (2007), the sensitivity of the Re number is more crucial when conical vortices occur around the bluff body, i.e. when the wind direction is e.g. 45°and not 0°, as in this case. Here, the Reynolds number was calculated, using the reference height (H) and the reference velocity u_H, to be $Re_H = 2.4{\cdot}10^4$, complying with both of the criteria. However, Re number independence was further verified by performing tests, to be presented in the following sections (see Section 4.1), with $u_\infty = 10$ m/s i.e. a Reynolds number twice as high.

The scale factor was calculated according to Cook's method (Cook, 1978), equal to $M = 1{:}\ 300$. All in all, the properties of the simulated boundary layer are summarized below: (i) the power law exponent $\alpha = 0.28$, (ii) the aerodynamic roughness length $z_0 = 1.80$ mm, (iii) the friction velocity $u_* = 0.25$ m/s and (iv) a roughness Reynolds number Re* = 29 (≥5). The values of the calculated power law exponent $\alpha = 0.28$ and the full-scale aerodynamic roughness length ($z_{0,\ full\ scale} = 0.54$ m) correspond to an urban atmospheric boundary layer, i.e. the flow over an inner city centre (VDI 3783, 2000).

2.2. Model building

The model building is a cubic building made of Plexiglas with an edge length of $H = 110$ mm (see Fig. 2). In the middle of each side of the model building there is a vertical slit-shaped opening. Each opening has a height of 90 mm (h) and a width of 6 mm (w), which corresponds to 4.5% of the area of the side to which it belongs. During the present experimental procedure, one of the building's vertical faces was oriented perpendicular to the flow direction and openings on the windward and leeward walls were sealed, leaving openings only on the side walls, parallel to the flow (lateral openings). A rectangular vertical column (22 mm × 22 mm × 100 mm) is placed internally, at the centre of the building model with a double role. Firstly, as a hollow column, it conceals the pressure tap tubing leading to the roof, secondly, its presence affects the flow conditions inside the model building, providing more realistic conditions for a building with interior obstacles. The four vertical walls were constructed in the same manner: hollow walls with a thickness of 5 mm to conceal the tubes of the side wall pressure taps. Therefore, the internal building volume corresponded to 100 mm × 100 mm × 100 mm.

The decision to place an opening in the centre of each of the two lateral walls (on opposite façades) serves the purpose of studying a mechanism similar to that of a single-opening case. In configurations of this type, the instantaneous pressure field is the driving force for the time dependent changes of inflow and outflow through each opening. Limited studies in the literature have shed light on this area of research. Indicatively, Chu et al. (2011) investigated the shear-induced ventilation rate of an isolated building in a uniform flow environment, while Ikegaya et al. (2019) focused on determining the velocity field around a cubic building sheltered by urban-like arrangements. Recently, Kobayashi et al. (2022) performed LES simulations for several cases of single- and double lateral-side openings to obtain information on the relationship between the effective ventilation rate and the bulk airflow rate for such cases.

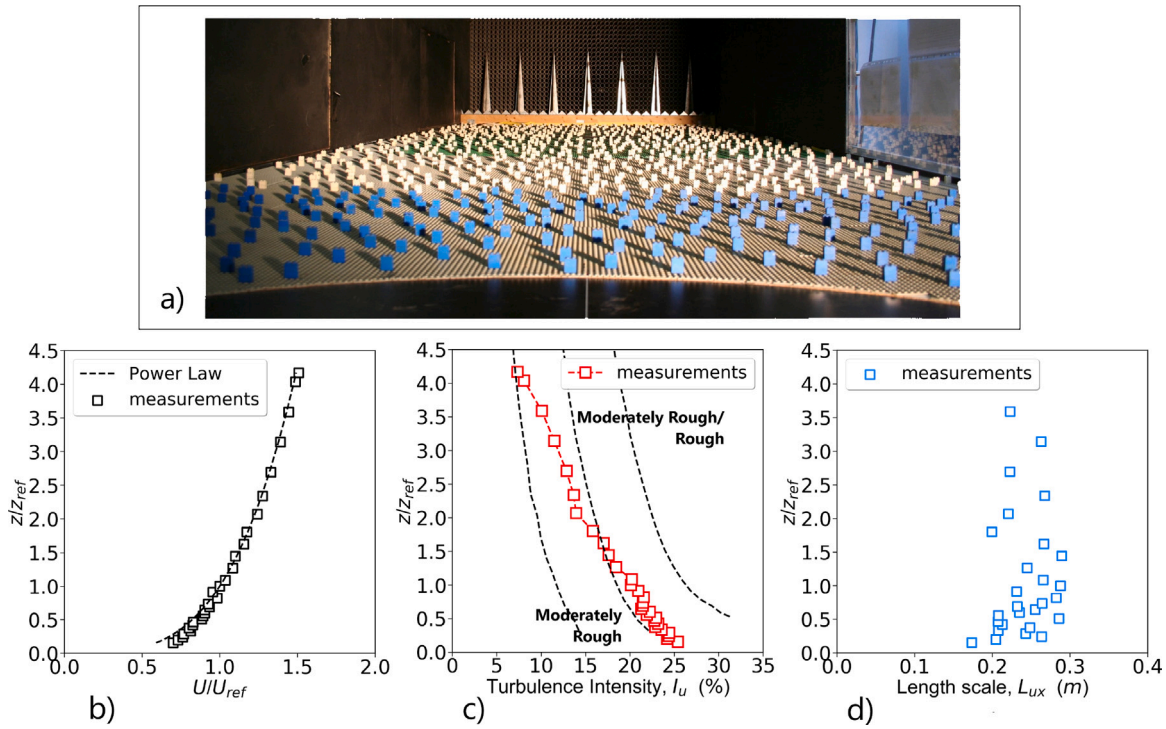

Fig. 1. (a) Set up of the fetch of the atmospheric boundary layer (ABL) upstream of the turntable. (b) measurements of the ABL profile and the fitting power-law for the velocity profile, (black square: measured wind velocity $u(z)$, black dashed line: power-law wind profile). (c) red square: calculated turbulence intensity, I_u, (d) blue square: calculated integral length scale, L_{ux}.

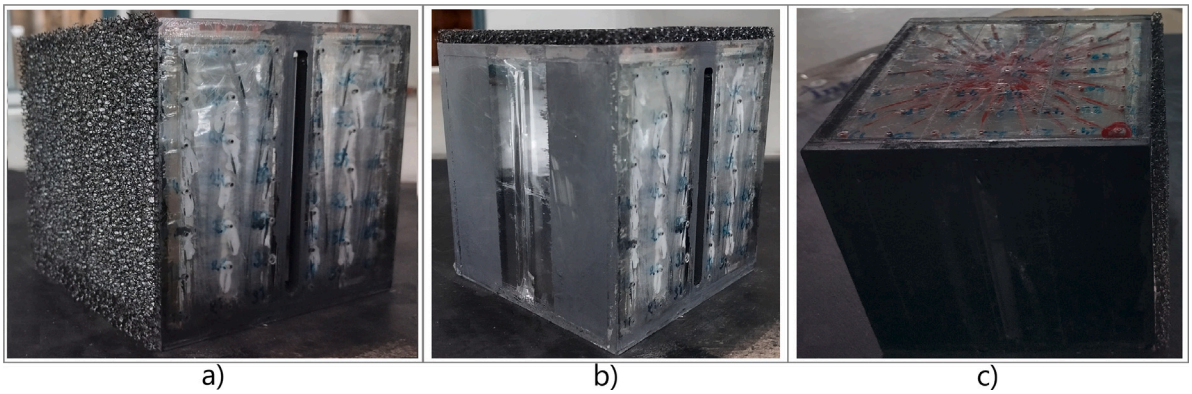

Fig. 2. The building model including side and roof pressure taps when tested for (a) façade greening with (λ_{fs} = 1.56 m^{-1},T$_L$), (b) rooftop greening with (λ_{fs} = 1.56 m^{-1},T$_L$) and (c) without vegetation.

Fig. 2 presents photographs of the model building, including the pressure tap distribution on the side wall (Fig. 2a–b) and on the roof (Fig. 2c). Fig. 3 provides the positioning of the pressure taps on the side wall and on the roof. It should be noted that only one outer face of the model building was fitted with a grid of 6 × 7 pressure taps, while its top face (roof) was covered with a grid of 7 × 7 pressure taps, which did not extend over the whole surface of the roof. Measurements on all vertical building faces were obtained by rotating the model and the same rotation procedure ensured that the pressure distribution on the whole roof was measured.

Pressure measurements were carried out for three different experimental configurations which are shown in Fig. 6:

(1) Bare building i.e. model building without greening (reference configuration, see Fig. 6a)
(2) Façade greening i.e. model building where the windward surface wall was fully covered with vegetation ($A_{coverage}$ = 100%, see Fig. 6b)
(3) Rooftop greening i.e. model building where the external surface of the roof was fully covered with vegetation ($A_{coverage}$ = 100%, see Fig. 6c)

2.3. Modelling vegetation in reduced-scale experiments

Vegetation is a complex porous medium consisting of stems, branches and leaves which affect the flow through the medium. This differs significantly from the flow around solid bluff bodies, which do not permit through-flow. Therefore, the principles and similarity criteria used in classical bluff body aerodynamics cannot be directly applied to the modelling of vegetation (Gromke, 2011). Based on previous experimental studies (Gromke et al., 2016; Pappa et al., 2023), our aim was to model the vegetation without focusing on modelling a specific tree species/kind with a "1 to 1" match, but to choose a material whose properties represent typical values of the vegetation, frequently meet in the literature. Among others, porous

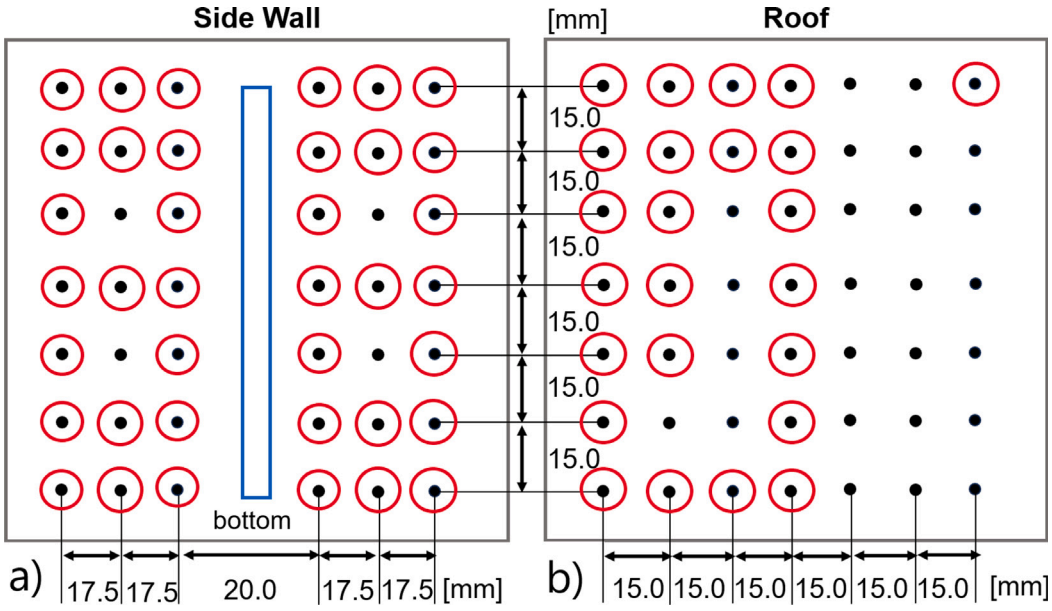

Fig. 3. Positioning of the pressure taps (a) on the side wall of the building (42 taps, black dots - 38 red circles represent taps where pressure measurements were recorded), shown in Fig. 2a–b and (b) on the roof (49 taps, black dots - 24 red circles represent taps where pressure measurements were recorded), shown in Fig. 2c.

foam is considered a representative material that fulfils this purpose. In the present experimental study, open-cell reticulated foams were used to model shrubs and ivy greening, two typical kinds of vegetation, suitable for rooftop and façade greening, respectively. Deformation and the geometrical shape of the vegetation was not taken into account in the modelling. The reduced scale modelling of vegetation requires the determination of four important properties: (*i*) the pressure loss coefficient, λ (m^{-1}) (*ii*) the leaf area density, LAD (m^2 m^{-3}) (*iii*) the porosity, ϵ (%) and (*iv*) the dynamic similarity law. In the following section, the aforementioned parameters are presented, their calculation method is analysed and, finally, a comparison is made between the model and real vegetation.

2.3.1. Determination of pressure loss coefficients

The present experimental study utilizes four different polyurethane foams: PPI60, PPI30, PPI20, and PPI10, at two different layer thicknesses: 5 mm (T_L) and 10 mm (T_{2L}). The acronym PPI stands for the number of Pores Per linear Inch, which is a typical measure for porous materials. It is generally recognized that the pressure drop through a porous medium at high velocities follows the Darcy–Forchheimer equation (Dukhan and Minjeur, 2011):

$$\frac{\Delta P}{T} = \frac{\mu}{K}U + \rho C U^2 \tag{1}$$

where ΔP is the pressure drop, T is the thickness of the porous medium in the flow direction, μ is the viscosity of the fluid medium, K is the permeability of the porous medium, ρ is the density of the fluid medium, U is the velocity in the flow direction and C is the form drag coefficient. In order to determine the pressure drop coefficient, separate experiments were carried out in an open-loop wind tunnel, at NTUA, under forced-convection flow conditions (see Fig. 4). Only the pressure loss coefficients of PPI30, PPI20 and PPI10 at thickness T_{2L} = 10 mm had already been determined earlier (Klausmann and Ruck, 2017).

The steady-state, unidirectional, static pressure difference (Δp_{static}) between two positions, upstream ($p_{windward}$) and downstream ($p_{leeward}$) of all foams, was measured in a velocity range between 0–5 m/s for PPI60 and at least between 0–8 m/s for the other foams, with an increment of 0.5 m/s. The measurements were repeated three times for each sample and the average of the three runs was determined. To eliminate any possible effects of the frame, the same procedure was repeated without the foam material, i.e. only for the wooden frame. The differences between the two procedures were considered to be the pressure drop values of the individual foams tested and are shown in Fig. 5. The measured pressure drop as a function of velocity is typical of pressure drop data for porous media (Dukhan and Minjeur, 2011; Boomsma and Poulikakos, 2002). The estimation of the uncertainties of the parameters of the curve fitting equation applied to the experimental data is based on the method of Antohe et al. (1997). The maximum uncertainties of the permeability of the porous medium, K are 7% while the corresponding uncertainties of the form drag coefficient, C are 14.4%.

The fitting showed that, for the conditions considered here, the linear term of Eq. (1) may be considered negligible. The pressure loss coefficient λ, is calculated as the coefficient of the quadratic term, determined from the Darcy–Forchheimer relation (Eq. (1)) for the entire velocity range (Dukhan and Patel, 2011) and multiplied by 2, to be compatible with the definition of Gromke and Ruck (2012) as given below:

$$\lambda = \frac{\Delta p_{static}}{p_{dynamic} T} \Rightarrow \lambda = \frac{p_{windward} - p_{leeward}}{\frac{1}{2}\rho U^2 T} \tag{2}$$

The calculated values of the pressure loss coefficients λ of the tested foams in reduced-scale experiments are included in Table 1. From here on, the values of the pressure loss coefficients measured in the wind tunnel are symbolized as λ_{rs} (reduced scale). In the next Section 2.3.2, the dynamic similarity law of vegetation is presented. Applying this criterion, the full-scale pressure loss coefficients, λ_{fs} of the porous medium are calculated and compared with the pressure loss coefficients of real vegetation. This comparison is based on an experimental study by Grunert et al. (1984) whose pressure loss coefficient values are shown in Table 2, while the analytical comparison method is described in Section 2.3.3.

2.3.2. Similarity law considerations

In the present modelling concept, the similarity criterion has been established based on momentum considerations. The basic assumption (Gromke and Ruck, 2012; Gromke et al., 2016; Pappa et al., 2023) of the aerodynamic similarity entails that the ratio of the momentum absorption by the vegetation (porous body) (drag force, F_d) over the momentum of the approaching wind flow (wind force, F_w) should be

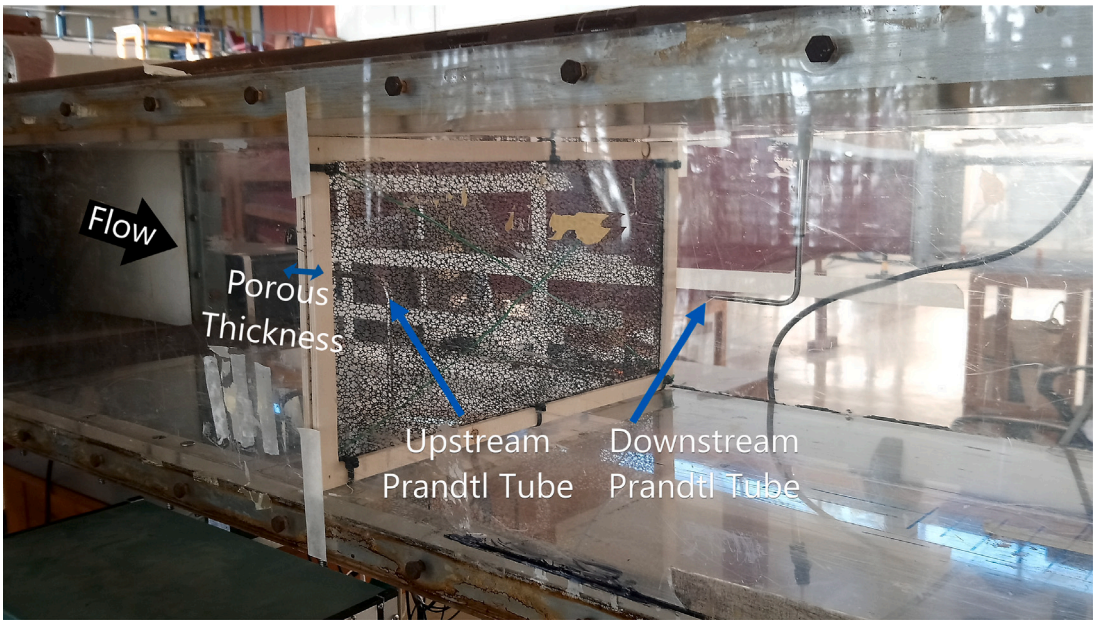

Fig. 4. Determination of pressure loss coefficient λ (m^{-1}), in forced-convection flow conditions.

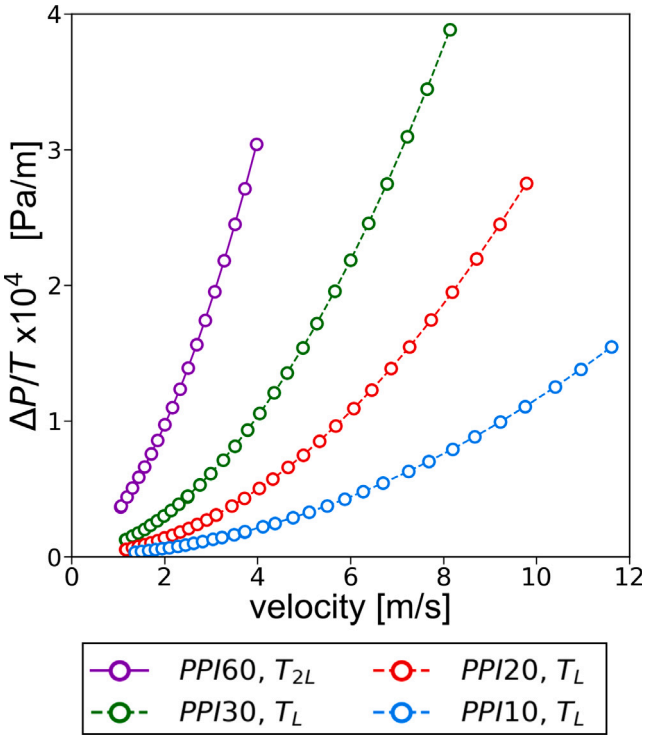

Fig. 5. Pressure drop as a function of velocity range of the four foam samples : (a) PPI60,T_{2L} (purple), (b) PPI30,T_L (green), (c) PPI20,T_L (red) and (d) PPI10,T_L (blue).

the same at both reduced-scale (rs) and full-scale (fs). This can be expressed as:

$$\left(\frac{F_d}{F_w}\right)_{rs} = \left(\frac{F_d}{F_w}\right)_{fs} \tag{3}$$

Under forced-convection flow conditions, as the ones described in the pressure drop measurements (see Section 2.3.1), Eq. (3) can be written as :

$$\left(\frac{\Delta p A_{cs}}{p_{dynamic} A_{cs}}\right)_{rs} = \left(\frac{\Delta p A_{cs}}{p_{dynamic} A_{cs}}\right)_{fs}$$
$$\Longleftrightarrow \left(\frac{\Delta p}{p_{dynamic}}\right)_{rs} = \left(\frac{\Delta p}{p_{dynamic}}\right)_{fs} \tag{4}$$

where A_{cs} is the cross-sectional area of the porous body normal to the flow. Based on the definition of the pressure loss coefficient, λ (m^{-1}) (see Eq. (2)) the last equation becomes:

$$\left(\frac{\lambda_{fs}}{\lambda_{rs}}\right) = \left(\frac{T_{rs}}{T_{fs}}\right) = M = 1:300 \tag{5}$$

where M is the geometric scale factor, as defined in Section 2.1. It is reiterated that through Eq. (5), the full-scale pressure loss coefficients, λ_{fs} and the full-scale vegetation thicknesses, T_{fs} can be extracted. These are shown in Table 1 and will be evaluated through comparison to actual values for vegetation in the next section.

2.3.3. Determination of leaf area density

The aerodynamic characterization of vegetation is not only based on the pressure loss coefficients λ (m^{-1}) but also on the leaf area density values LAD (m^2 m^{-3}). These two parameters are connected through the equation:

$$\lambda = LADC_d \tag{6}$$

where C_d is the drag coefficient of a vegetation element. Typical values of leaf drag coefficient C_d are in the range of 0.1–0.5 (Buccolieri et al., 2018). In the present study and as successfully applied in the past (Pappa et al., 2023), a representative drag coefficient C_d was chosen to be 0.3 (Ysebaert et al., 2022).

The combination of Eqs. (5) and (6) determines the full-scale leaf area density, LAD_{fs}. Table 1 summarizes the vegetation parameters for all cases investigated. The lower and upper limits of the obtained pressure loss coefficients λ_{fs} and leaf area density LAD_{fs} at full scale are between (0.65–7.82) m^{-1} for the first parameter and (2.2–26.1) m^2 m^{-3} for the second. These up-scaled values are compared with literature data from the study of Grunert et al. (1984) as previously performed by Gromke (2011), Gromke et al. (2016), Gromke (2018) and Pappa et al. (2023). In Grunert et al. (1984), different leaved and leafless shrubs were tested under forced-convection flow conditions

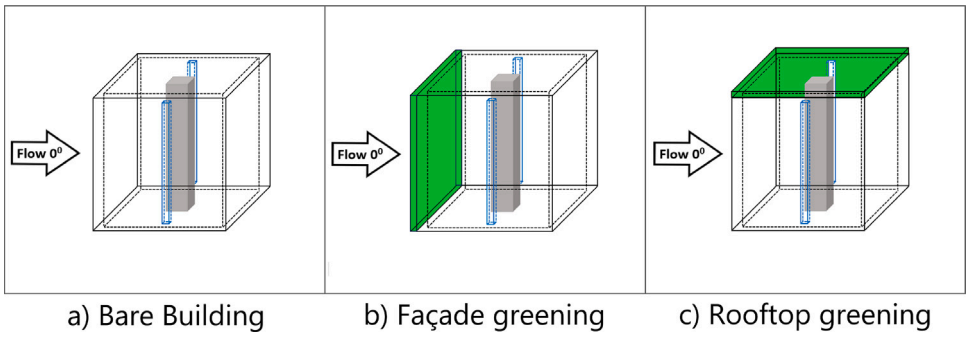

Fig. 6. Total tested experimental configurations: (a) Bare building (without greening), (b) Façade greening and (c) Rooftop greening.

and the results are presented in Table 2. The pressure loss coefficients λ (m^{-1}) are shown for selected vegetation species and per branch density, ρ_b. The branch density, ρ_b is defined as the density of the branch arrangement during the experimental procedure, where 1.0 is the normal density, ≤1.0 is the thinner density and ≥1.0 is the thicker density. By comparing the full-scale pressure loss coefficients λ_{fs} of Table 1 with the pressure loss coefficients λ of Table 2, an overall agreement can be seen. Nevertheless, Eq. (5) states that the product of vegetation layer thickness and pressure loss coefficient is the decisive scaling criterion for aerodynamic similarity and not each of them separately. The multiplication of λ_{fs} with T_{fs} i.e. T_L = 1.5 m (to be referred to as thin vegetation species) and T_{2L} = 3.0 m (to be referred to as double or thicker vegetation species), attribute values that lay in the range of (1.0–4.6) for thinner vegetation and (2.5–23.5) for thicker vegetation respectively. Again, the comparison with the results of Grunert et al. (1984) is satisfactory, with the only exception being the extreme case of thicker vegetation species (λ_{fs} = 7.82 m^{-1}, T_{2L}).

An alternative approach, more relevant to ivy greening, is based on the concept of the leaf area index, LAI (m^2 m^{-2}) i.e. the leaf area per unit ground or trunk surface area of a plant (Pérez et al., 2022). The LAI values that are suitable for façade greening (ivy greening) as a passive tool for energy saving in buildings have been found to be between (0.24–5.0) m^2 m^{-2}, although values between (3.0–5.0) m^2 m^{-2} are most preferable (Pérez et al., 2022). LAI is related to LAD through the vegetation thickness i.e. LAI = LAD·Thickness. Based on this, the calculated LAD values for real ivy greening are between (3.0–19) m^2 m^{-3}, for a thickness range between 0.5 m and 1.5 m. The comparison with the LAD_{fs} values of Table 1 shows that all tested foams in both thicknesses are compatible with the real vegetation data, with the exception of the thicker PPI60 foam.

2.3.4. Porosity measurements

Porosity measurements of the utilized foam material were carried out in order to assess their agreement with the porosity of real vegetation crown layers. The porosity measurements were performed with a portable optical digital microscope. The digital images were acquired and processed using digital image processing software (Karoglou et al., 2013). The porosity was also determined by measuring the apparent and real density of the foams. The measured porosity values of the individual porous foams and their uncertainties are included in Table 1. It is clear that the porosity value, ϵ of the denser PPI60 foam corresponds to 96.50% while the values for the other foams are approximately 97.30% ±0.30. These measured porosity values of polyurethane foams with different pores per inch (PPI) agree with the corresponding pore volume fraction values, P_{vol} of deciduous crown porosities. Specifically, according to Ruck and Schmidt (1986), two average values were determined for the pore volume fraction: P_{vol} = 96.00% as low crown porosity and P_{vol} = 97.50% as high crown porosity.

2.3.5. Discussion

In summary, the tested polyurethane foams are suitable for modelling vegetation in reduced-scale experiments as they successfully meet the requirements for dynamic similarity to real vegetation data in terms of pressure loss coefficient λ, leaf area density LAD and the product of pressure loss coefficient and thickness ($\lambda \cdot T$). Despite the fact that PPI60 exceeds the limit values for all of the above parameters, its application was taken into account in the surface pressure measurements on the model building as it was considered an extreme case, i.e. the upper threshold of greening effects on the model building. However, one could argue that the thickness of adopted vegetation layer and especially in the case of greening wall is not geometrically representative of a real one. It is true that in the simplest case, vegetation covering a wall may be quite thin and in the range of several cm. Although, in the more general and recent sense, the green wall maybe in the form of two different systems, the green façade and the living wall. The difference between the green façade and living walls is that in the first case, the vegetation is rooted in the ground, climbing up the façade and covering the height, while living walls consist of pre-vegetated plants and cladding structures that provide a variety of plants to cover the building façade evenly (Besir and Cuce, 2018) This means that the green façade can consist of either trees or ivy vegetation. The scale factor of our wind tunnel study is 1 : 300 and we tested two different thicknesses of 5 mm and 10 mm. In full scale, this corresponds to a vegetation thickness of 1.5 m and 3 m. While a width of 3 m can be an extreme case for trees, and this also applies to ivy, these values are within generally accepted frameworks (e.g. Urban Forestry (Vertical Forestry), Stefano Boeri Architetti (2014)), which recommends trees, shrubs/bushes and ivy up at a width of ≥1.0 m. These scales are also consistent with other studies such as that of Li et al. (2022) who experimentally investigated the effects of 1.6 m thick green walls on the ventilation and heat removal from street canyons. In the present approach to vegetation modelling, the dynamic behaviour of the vegetation has not been directly taken into account. It is true that tree leaves, branches and the whole greening, reduce their cross-sectional area normal to the flow by bending and twisting and thus become more streamlined and compact. These are counter-acting effects, as the streamlining will reduce the drag force, while at the same time the lower porosity of the more compact foliage will increase it Gosselin (2019). However, these deformation effects are dominant at higher velocities (Manickathan et al., 2018; Bekkers et al., 2022), well above usual near-ground wind velocities of the atmospheric boundary layer, where the wind flow interacts with the vegetation (either façade greening or rooftop greening). Therefore, it can be argued that our experiments cover typical wind conditions that prevail most of the time. There are wind conditions in which deformations exist, but they are rather rare. As the air exchange scales with the wind speed, the high wind velocity periods are rather uncritical in terms of indoor air quality (European Environment Agency, 2024). Regarding the compaction of vegetation at high(er) wind speeds, one may argue that the related effects are qualitatively represented in the lower permeability

Table 1
Experimental results of the tested foam material for modelling vegetation parameters: pores per inch of foam samples, porosity, ϵ (%), foam thickness at reduced scale T_{rs} (mm) and at full scale T_{fs} (m), pressure loss coefficients at reduced scale λ_{rs} (m^{-1}) and at full scale λ_{fs} (m^{-1}), the product of pressure loss coefficients and the corresponding thickness at full scale, (–) and leaf area densities at full scale, LAD_{fs} (m^2 m^{-3}).

Foam (pores per inch)	Porosity, ϵ (%)	Reduced scale thickness, T_{rs} (mm) full scale thickness, T_{fs} (m)	λ_{rs} (m^{-1})	λ_{fs} (m^{-1})	λ T (–)	LAD_{fs} (m^2 m^{-3})
PPI60	96.58 ±0.11[a]	T_{2L} = 10 mm/3.0 m	2346	7.82	23.5	26.1
PPI30	97.15 ±0.10[a]	T_{2L} = 10 mm/3.0 m	1000	3.33	10.0	11.1
PPI20	97.30 ±0.12[a]	T_{2L} = 10 mm/3.0 m	500	1.67	5.0	5.6
PPI10	97.55 ±0.15[a]	T_{2L} = 10 mm/3.0 m	250	0.83	2.5	2.8
PPI30	97.15 ± 0.10	T_L = 5 mm/1.5 m	913	3.04	4.6	10.1
PPI20	97.30 ± 0.12	T_L = 5 mm/1.5 m	468	1.56	2.3	5.2
PPI10	97.55 ± 0.15	T_L = 5 mm/1.5 m	194	0.65	1.0	2.2

[a] Indicates values measured for same material at different thickness.

Table 2
Grunert et al. (1984) experimental pressure loss coefficients λ (m^{-1}), under forced-convection flow conditions, for a variety of real leaved shrubs.

Branch density, ρ_b	1.33	1.00	0.67	Thickness, T (m)
Small-leaved lime	1.5–4.0	0.9–2.3	0.4–1.5	1.0
Bird cherry	1.5–13.4	1.2–6.5	0.6–3.1	1.0
Poplar	1.2–3.6	0.8–2.4	0.5–1.5	1.0
Norway maple	1.5–3.5	1.1–2.5	0.7–1.6	1.0
Field maple	4.7–8.9	3.5–6.9	2.2–4.0	1.0

cases (which at the same time represent the same vegetation species). However, this remains a pure qualitative consideration as we are not able to relate the degree of compaction of the greening with wind speed.

3. Pressure measurement procedure: set-up and signal analysis

3.1. Pressure measurement set-up and accuracy

The pressure measurements include the steady and unsteady pressure distributions on the outer surfaces of the model building. During the experimental procedure, two miniature pressure scanners (type ESP-32HD, PSI Pressure Systems), each with 32 piezoresistive silicon differential pressure transducers, were used and recorded by a data acquisition system (type DTC Initium, PSI Pressure Systems). The scanners were connected to 0.6 mm diameter pressure taps on the model building surfaces with tubing comprising, for each tap, a first section of 0.4 m long silicone tube with a 0.5 mm inner diameter and a second section of 0.6 m long tube with a 1.0 mm inner diameter. Although a total of 42 pressure taps on the side wall and 49 on the roof (black dots in Fig. 3) were available, due to equipment restrictions, only 64 taps could be recorded simultaneously i.e. 38 pressure taps on the side wall and 24 pressure taps on the roof (red circles in Fig. 3a and b, respectively). One tap was reserved for the static reference pressure (p_o) and one more tap for the dynamic pressure ($p_{dynamic}$) in the free stream. The choice of measurement positions took advantage of the fact that, by rotating the model, the full area of the roof would be successfully captured. Alignment of the building with respect to the flow (i.e. symmetry of the flow) was checked by comparing the pressure signal from at least two symmetrical taps on the roof.

The sampling frequency f_s during the experimental procedure was set to f_s = 1 kHz for an acquisition time of t_{ac} = 120 s. Given that the integral time scale, calculated from the measurements of the upstream flow, was T_{ux} = 0.12 s at the height of the model building, this means that the acquisition time nominally includes 1000 passages of the largest eddy structures. The measuring range of the pressure transducer is ±2500 Pa, but during the present pressure measurements, the measured pressures did not exceed 64 Pa, for the highest Re number. Based on a recent calibration protocol for the employed pressure scanner system, provided by a certified calibration institute, the maximum error in the measurement range of ±70 Pa was ±0.08 Pa, corresponding to ≤0.12% of this range of interest. For calculations of the total uncertainties, thermal and acquisition errors were also taken into account at 0.004% FSO per °C degree and 0.003% FSO, respectively, as provided by the manufacturer. Total pressure uncertainty was calculated as the square root of the sum of the squared individual errors, for each pressure tap position. The average relative uncertainty of the pressure measurements was 5%, with a limited number of higher values in the low pressure regions on the back of the model building. In addition, the uncertainties of the pressure coefficients were calculated using the error propagation law, taking into account the uncertainties of the pressure measurements per tap, the uncertainty of the u_H based on the hotwire measurements, i.e. 3% and the uncertainty of the air density, i.e. 0.01%. The average relative uncertainty of the pressure coefficients was 6.2%, with a limited number of higher values (11%) in the leeward building wall. The analytical calculations are available but not included for lack of space.

Although the internal pressures and its modelling in scaled geometries is not within the scope of the present study, it may have an effect on the pressure difference across an opening through which there is an air exchange. Correct scaling of the internal volume should therefore be taken into account when performing a scale model simulation. Holmes (1979) has shown that the internal volume behaves similarly to a Helmholtz resonator with internal pressure fluctuations arising due to compressibility effects of the fluid. He also showed that, in scale model studies, geometric scaling of the whole model may not be sufficient to maintain similarity of the dynamic response of the internal volume. Internal volume scaling requires (Holmes, 1979) :

$$V_{ms} = V_{fs} \frac{\left(\frac{L_{ms}}{L_{fs}}\right)^3}{\left(\frac{U_{H_{ms}}}{U_{H_{fs}}}\right)^2} \tag{7}$$

where L is a characteristic length, V is the internal volume, U_H is the mean wind speed at roof height and the indices *ms* stand for the model scale and *fs* for the full scale, respectively. For the velocities of our study (i.e. U_∞ = 5 m/s and $U_{H_{ms}}$ = 3.27 m/s), a velocity scale of $U_{H_{ms}}/U_{H_{fs}} = 1:1$ is considered, so Eq. (7) shows that no scaling, other than the geometric scaling L_{ms}/L_{fs} is required. The choice of a velocity scale of 1:1 is based on data from the European Environment Agency (2024) which gives the mean wind speed of 2.5 m/s at 10 m height per year, for Southern Europe. This mean wind speed is fairly close to the full-scale equivalent of our wind tunnel experiments for which $U_{10m_{fs}}$ = 2.34 m/s.

3.2. Pressure signal analysis

A transfer function to compensate for amplitude damping or gain corrections and phase shift distortions through the tubing was applied to the pressure signal based on Bergh and Tijdeman (1965). In addition, a low-pass IIR (IIR: Infinite Impulse Response) Butterworth filter of 10th order with a cut-off frequency of f_{co} = 100 Hz was applied in a pre-processing step of the pressure time series. The choice of 100 Hz as the lower threshold value is due to the insignificant contributions of higher

Table 3
Total pressure measurements of the three experimental configurations as acquired on the four outer surfaces of the model building: windward wall, side wall, leeward wall and roof face.

Bare building △	Façade greening □		Rooftop greening ○	
Inflow (0°)	Windward wall	Side wall	Leeward wall	Roof face
Bare building	△	△	△	△
λ_{fs} = 7.82 m^{-1} , T_{2L}	/ ○	□ / ○	□ / ○	□ / ○
λ_{fs} = 3.33 m^{-1}, T_{2L}	/ ○	□ / ○	□ / ○	□ / ○
λ_{fs} = 1.67 m^{-1}, T_{2L}	/ ○	□ / ○	□ / ○	□ / ○
λ_{fs} = 0.83 m^{-1}, T_{2L}	/ ○	□ / ○	□ / ○	□ / ○
λ_{fs} = 3.04 m^{-1}, T_{L}	/ ○	□ / ○	□ / ○	□ / ○
λ_{fs} = 1.56 m^{-1}, T_{L}	/ ○	□ / ○	□ / ○	□ / ○
λ_{fs} = 0.65 m^{-1}, T_{L}	/ ○	□ / ○	□ / ○	□ / ○

frequencies ($100 \leq f \leq 500$) to the power spectrum density of the raw, unfiltered pressure signals.

The mean pressure coefficients, Cp_{mean} and the fluctuating pressure coefficients, Cp_{fluct} were calculated for the differential, with respect to the upstream static pressure, filtered time series pressure signal. The mean dynamic pressure at the height of the model building (based on the reference velocity u_H as measured during the simulation of the atmospheric boundary layer, see Section 2.1), was used for the calculation of both pressure coefficients.

One way of quantifying the effects of vegetation on the pressure coefficients was to compare them with the bare building (without greening) using relative differences. The ΔCp_j relative differences were calculated as:

$$\Delta Cp_j = \frac{Cp_j^{greening} - Cp_j^{Nogreening}}{Cp_j^{Nogreening}} \tag{8}$$

where j stands for *mean* or *fluct*, respectively.

Moreover, the non-dimensional power spectrum density of the instantaneous pressure signal, which is presented in Section 4.6, measured at six different side wall pressure taps at mid-building height was calculated, applying the Welch method (Welch, 1967). All the investigated cases are summarized in Table 3.

4. Results and discussion

This section presents the results of the post-processing analysis of the surface pressure measurements on the exterior walls of the model building with and without vegetation. First, in Section 4.1 the sensitivity of the Reynolds number for selected cases of pressure measurements is investigated, while in Section 4.2 a validation with the widely recognized Silsoe cube, field experiment is performed. Section 4.3 analyses the bulk effects of façade and rooftop greening on the pressure distribution, while Section 4.4 focuses on the quantitative comparison of the greening position with the bare building case. In Section 4.5, the emphasis is on the façade greening, which shows the more prominent effects related to the air exchange mechanisms near the openings. Façade greening layers with different pressure loss coefficients, thicknesses and the same overall pressure drop $\lambda_{fs} \cdot T_{fs}$ are tested. Finally, in Section 4.6, the effect of the façade greening is further explored using a frequency spectrum analysis of the pressure fluctuations along the side wall.

4.1. Reynolds number sensitivity of pressure measurements

In order to investigate the Reynolds number sensitivity of the pressure measurements, these were performed for the atmospheric boundary layer approach flow with two free stream velocities: u_∞ = 5 m/s and u_∞ = 10 m/s. The corresponding Reynolds numbers based on the reference height (H) and the reference velocity u_H, were $Re_H = 2.4 \cdot 10^4$ (as already analysed in Section 2.1) and $Re_H = 4.7 \cdot 10^4$, where the reference velocity at building height is equal to u_H = 6.84 m/s. The Reynolds number sensitivity measurements were performed for three different configurations: (*i*) bare building, (*ii*) windward façade greening and (*iii*) rooftop greening. The material in both greening configurations corresponded to λ_{fs} = 1.67 m^{-1}, T_{2L}. Results for the mean pressure coefficients, Cp_{mean} are presented in Fig. 7a, for the bare building configuration, along a horizontal line at building mid-height, and in Fig. 7b along the central vertical line. Fig. 7c–d show the mean pressure coefficients, Cp_{mean} for the façade and rooftop greening, respectively, along a horizontal line at building mid-height. Overall, this Reynolds number sensitivity of bluff bodies covered with porous foam on the surface walls has novel elements, as it is the first time that this has been tested and presented in the literature. There are experimental studies dealing with pressure measurements on airfoils/wings with porous medium (Aldheeb et al., 2018) or on porous airfoils (Tamaro et al., 2021) manufactured with known porosity. There are also studies that deal with the effects of porous circular cylinders on the drag coefficient (Klausmann and Ruck, 2017) or the investigation of the wake of porous square cylinders (Ledda et al., 2018; Seol et al., 2024). However, as far as the authors are aware, there is no mention in the literature to date addressing the Reynolds effects on the external pressure field of sharp-edged bodies (such as a building) covered with porous material (of known and varying porosity and thickness). Findings show that there is no pronounced Reynolds number sensitivity at the wind speeds investigated, with differences in calculated pressure coefficients among the two Reynolds numbers of less than 5%. All the results presented in the following sections were obtained with the lower Reynolds number i.e. with u_∞ = 5 m/s.

4.2. Validation

Taking into account the results from Section 4.1, a validation test of the model building with closed openings is performed in comparison to literature data. The field measurement of the Silsoe cube (Richards and Hoxey, 2012) is a widely accepted case, frequently used for validation as it represents a realistic isolated building (6m edge length) with detailed surface pressure measurements available. The pressure measurements with a free stream velocity of u_∞ = 5 m/s, having the same atmospheric boundary layer inflow as described in Section 2.1 were used for the comparison. The distribution of the mean (Fig. 8a) and fluctuating (Fig. 8b) pressure coefficients is shown along a horizontal line, that includes the windward, the side and rear walls, at mid-building height. The values of the Silsoe cube were adjusted accordingly to be compatible with the definition in Section 3.2. The comparison between the wind tunnel data and the Silsoe cube shows encouraging agreement in both the mean and fluctuating pressure coefficients, particularly on the windward and on the side walls (area of high gradients), especially where the separation mechanism and the reattachment bubble occur. On the rear wall, both the mean and the fluctuating pressure coefficients remain almost constant, but the mean suction of the Silsoe cube is larger and fluctuations are almost twice as high. It should be noted that the rear wall is a region of low pressures where the measurement uncertainties are higher but it is also a region far from the side walls, where most of the interest of the current study lies. Furthermore, the Silsoe cube is exposed to a rural terrain with a mean velocity profile exponent of α_{Silsoe} = 0.17, which is probably the decisive factor for quantitative differences.

4.3. Bulk effects of rooftop and façade greening on surface pressure distribution on the model building

From the pressure measurements, a clear picture of the pressure distribution on the building's outer surfaces can be derived. In Figs. 9 and 10, the distributions of the mean pressure coefficient, Cp_{mean} and its fluctuation, Cp_{fluct} on the outer building surfaces are presented for the case of the building without vegetation (Fig. 9a, Fig. 10a), the building with façade greening (Figs. 9b, 10b) and the building with rooftop

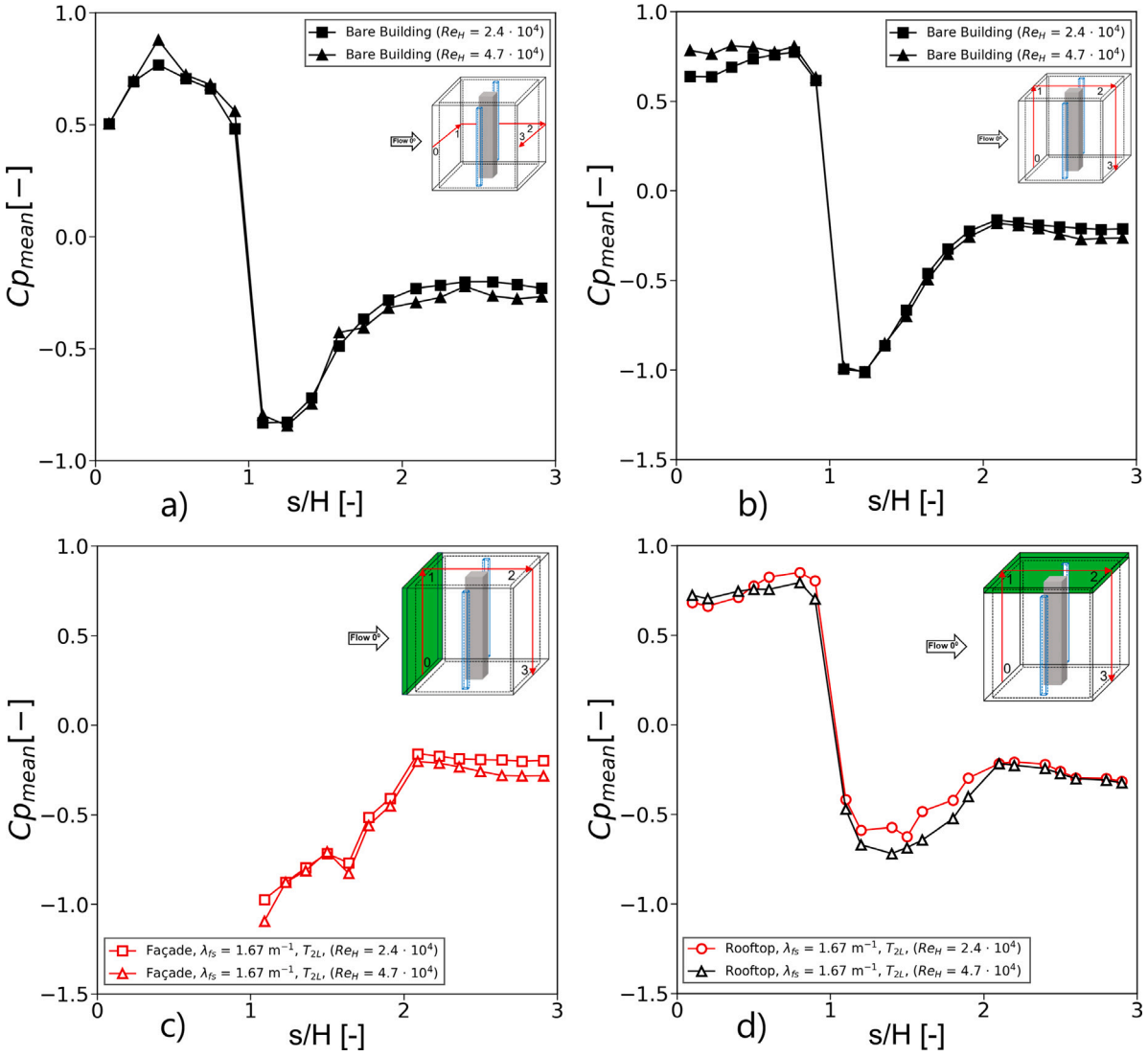

Fig. 7. Mean pressure coefficients, Cp_{mean} at two Reynolds numbers: $Re_H = 2.4 \cdot 10^4$ and $Re_H = 4.7 \cdot 10^4$, for the bare building (a) along the horizontal line, at mid-height and (b) along the central vertical line, and along the central vertical line for (c) façade greening and (d) rooftop greening.

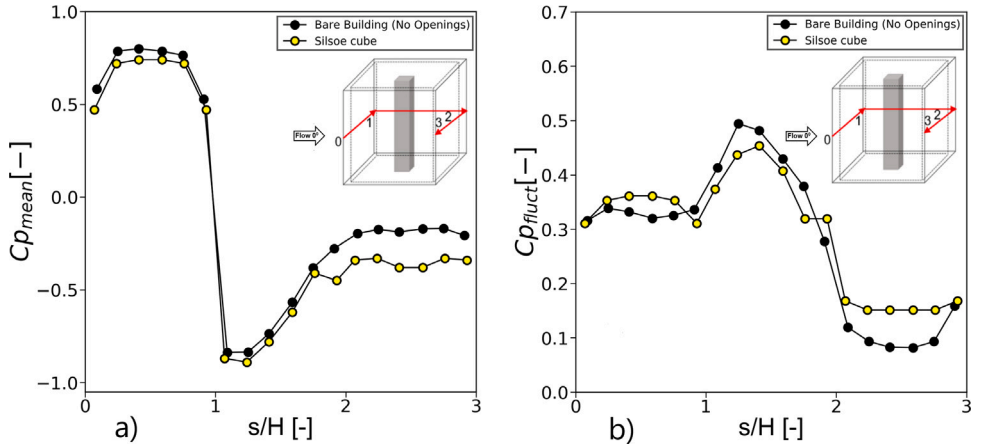

Fig. 8. (a) Mean pressure coefficients, Cp_{mean} and (b) fluctuating pressure coefficients, Cp_{fluct} of bare building without openings in comparison with Silsoe Cube (Richards and Hoxey, 2012), along the horizontal line, at mid-height.

greening (Figs. 9c, 10c). The vegetation case with λ_{fs} = 1.67 m^{-1}, T_{2L} is chosen to illustrate typical effects, avoiding the extreme cases of high pressure loss coefficient, λ_{fs} (low permeability, K) or thin greening layers. It should be noted that it was not possible to obtain pressure data underneath the greening layer in the façade greening case. A plausible explanation could be that the positive stagnation pressures caused the greening material to block the pressure tap orifices on the upstream face. This was not an issue for the case of rooftop greening, presumably due to the suction pressure occurring on the roof. From the mean pressure coefficients, the bare building's windward face stagnation point is located at roughly $^2/_3$ H from the ground and is surrounded by a pressure drop towards the horizontal and vertical edges (Fig. 9a). This is accompanied by a sharp drop in pressure on the roof and at the side wall upstream edges, due to flow separation. However, when rooftop greening is present, although the pressure drop on the side face is not significantly affected, the windward face's high pressure zone extends to the roof's leading edge (Fig. 9c) and, compared to the bare building case, the suction is relatively more homogeneous. Maximum suction occurs downstream and not at the roof leading edge. This can be attributed to the presence of rooftop greening, which is disrupting the separation of the flow from the leading edge and creating a region of increased resistance, compared to the case of the bare building. This is also observed from the increased value of upstream face stagnation pressure. Looking at the pressure fluctuation in the same areas, the high values covering the upper part of the windward face in the bare building case (Fig. 10a) seem to be restricted towards the roof's leading edge when rooftop greening is present and the rooftop pressure fluctuation is reduced (Fig. 10c). The effect on the side wall is significantly less pronounced.

Although it was not possible to measure below the vegetation layer in the façade greening case, it is possible to see the effects of façade greening on the roof and side wall. Again, the vegetation layer seems to be disturbing the separation mechanism on the leading edges, as with rooftop greening. The roof and side wall peak low pressure regions are restricted but, for the most part, the roof and the side walls do not have the prominent streamwise pressure gradients (Fig. 9b) of the bare building case (Fig. 9a). A similar observation can be made for the pressure fluctuation: whereas the bare building exhibits strong streamwise gradients of pressure fluctuations on both the roof and the side walls (Fig. 10a), when façade greening is present, the maximum fluctuation coefficients are reduced as are their spatial gradients on these surfaces and a more uniform distribution is present (Fig. 10b).

Overall, the data suggest that greening affects the way that the flow separates from the horizontal and vertical edges of the building's upstream face, thus affecting the extent and the mobility of the recirculation bubbles forming on the roof and the side walls. It is interesting to note that, comparing Fig. 9a with Figs. 9b and 9c, for the bare building and the rooftop greening cases, the mean pressure is almost uniformly distributed along the lateral openings. Thus, taking into account the symmetry among the two opposite openings, is not expected to significantly contribute any air exchange through the openings. Façade greening disrupts this uniformity of the mean pressure field to some extent but both the nature and the non-uniformity of the distribution of the pressure fluctuation along the openings (Fig. 10a compared to Fig. 10b and c) can be expected to dominate air exchange, as will be shown in the following sections.

4.4. Effects of greening position

In order to obtain a more quantitative understanding for the observations made from the surface pressure distributions, variations of mean and fluctuating pressure coefficients are presented as line plots along selected linear paths for two extreme cases of vegetation, namely λ_{fs} = 7.82 m^{-1},T_{2L} and λ_{fs} = 1.56 m^{-1},T_L and compared to those of the bare building.

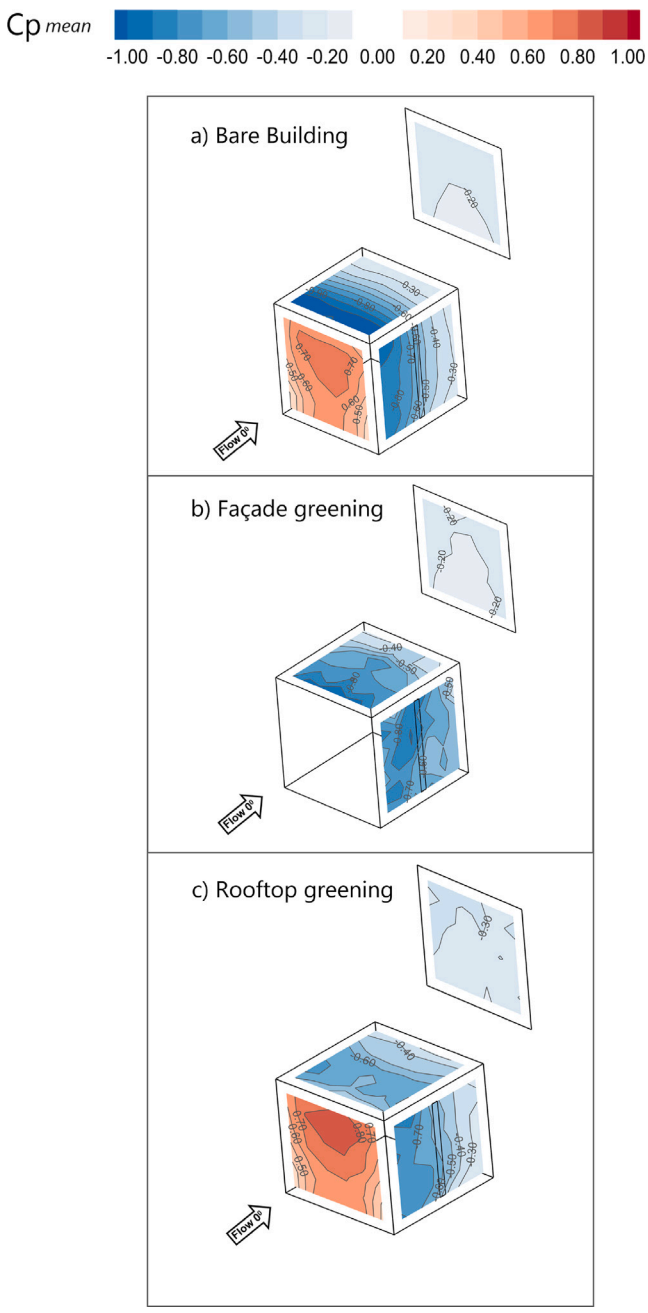

Fig. 9. Calculated distributions of mean pressure coefficients, Cp_{mean} of (a) bare building (without greening), (b) façade greening (λ_{fs} = 1.67 m^{-1},T_{2L}) and (c) rooftop greening (λ_{fs} = 1.67 m^{-1}, T_{2L}) configurations.

In Figs. 11 and 12, the mean and fluctuating, respectively, pressure coefficients are plotted along a horizontal path that spans the front, side and rear walls. Results are shown for the bare building as well as for the façade greening (Figs. 11a, 12a) and the rooftop greening (Fig. 11b, Fig. 12b). It is noted that these two greening layers differ in values of $\lambda \cdot T$ by one order of magnitude and therefore, if the velocity is the same, so will the pressure difference that they induce (see Eq. (2)). Along a mid-height horizontal pathline, the mean pressure coefficient Cp_{mean} of the bare building shows a maximum in the middle of the windward face, a slight drop towards the vertical edges and a significant drop downstream of the leading edge (s/H = 1) of the side wall (Fig. 11). The pressure drop on the side wall leading edge is associated with the flow separation occurring there. It leads to a suction (negative) pressure

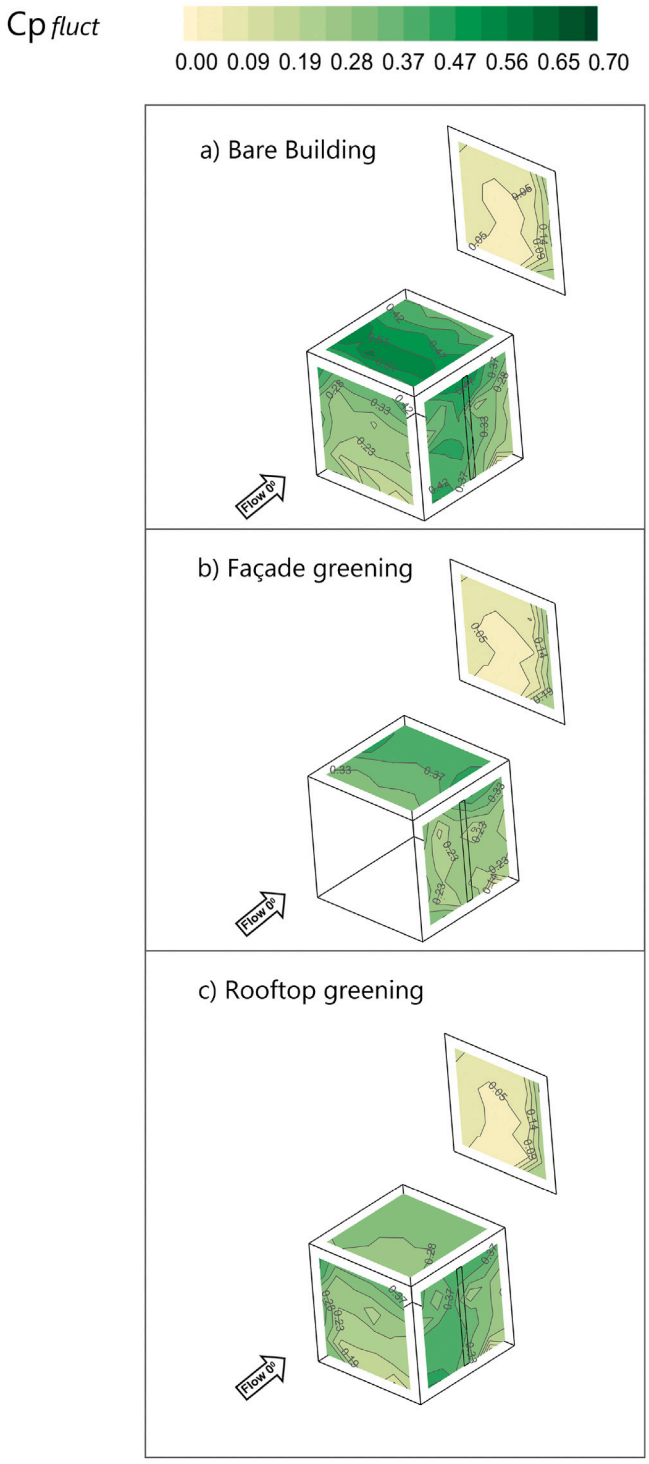

Fig. 10. Calculated distributions of fluctuating pressure coefficients Cp_{fluct} of (a) bare building (without greening), (b) façade greening (λ_{fs} = 1.67 m^{-1},T_{2L}) and (c) rooftop greening (λ_{fs} = 1.67 m^{-1},T_{2L}) configurations.

and although it quickly begins to recover along the side wall, it remains negative and retains an almost constant value on the downstream wall. Overall, the distribution is typical for this type of flow and in agreement with previous studies (Castro and Robins, 1977; Ciarlatani et al., 2023). The fluctuation pressure coefficient (Fig. 12) is fairly constant on the windward face with a slight drop near the edges.

On the side wall, travelling downstream from the windward vertical edge, Cp_{fluct} climbs to its maximum value upstream of the middle of the wall (s/H = 1.25) and the opening, before making a significant drop towards the leeward vertical edge. The pressure fluctuations are even lower on the leeward face. The high levels of fluctuating pressure on the side wall, near the leading edge, are indicative of the mobility of the separation bubble forming there (Pappa et al., 2019; Ciarlatani et al., 2023). It is however interesting to note that, these are significantly lower on the downstream half of the side wall.

For vegetation added to either the windward façade or the rooftop, the effect on the distribution of the mean pressure coefficient is presented in Fig. 11. Although there is a tendency to attenuate the side wall suction peak when façade greening is present (Fig. 11a), the maximum relative differences of the peaks are rather limited ($\Delta Cp_{mean\text{-}max.}$ ~−12.4% for λ_{fs} = 7.82 m^{-1},T_{2L} greening species). However, rooftop greening (Fig. 11b) has a more pronounced effect with a maximum difference of $\Delta Cp_{mean\text{-}max.}$ ~+33% on the windward face for λ_{fs} = 1.56 m^{-1},T_L greening species. This is possibly due to a flow retarding effect when the rooftop vegetation is present. In particular, in the case of the lower pressure coefficient, i.e. λ_{fs} = 1.56 m^{-1},T_L, the flow passes through the porous medium and is subject to its resistance so higher pressures are induced on the windward wall. For higher pressure coefficients, i.e λ_{fs} = 7.82 m^{-1},T_{2L}, the flow is presumably bypassing the vegetation layer with little effect on the pressure of the windward face of the building. Similar effects are observed for the leeward face, both for the façade ($\Delta Cp_{mean\text{-}max.}$ ~ 61%) and for the rooftop ($\Delta Cp_{mean\text{-}max.}$ ~ 60%) greening, for the thinner layer with low resistance i.e. λ_{fs} = 1.56 m^{-1},T_L. When evaluating these differences, one should keep in mind the very low pressure coefficients on the leeward face.

However, for the fluctuating pressure (Fig. 12), the presence of façade greening, regardless of thickness or permeability, leads to a pronounced drop (ΔCp_{fluct} ~35%) in the pressure coefficient on the upstream half of the side wall, compared to the case of the bare building. Again, the effect of both greening species is similar. For rooftop greening, the effect on pressure fluctuation is not evidently significant on either of the three faces, at least at the building's mid-height, where the present analysis is focused.

Looking at the mean and fluctuating pressure coefficients (Figs. 13 and 14, respectively) along a path that starts at the centre of the windward face's bottom edge and runs vertically up, then along the roof and down to the centre of the leeward face's bottom edge, a similar picture emerges. Significant effects on the mean pressure coefficient are only observed on the roof, where the largest relative differences are at the leading edge in the case of rooftop greening. Similar behaviour to the mean pressure coefficients is observed for the pressure fluctuations Cp_{fluct}, particularly on the roof when rooftop greening is present (Fig. 14b). However, they are also significant when façade greening is present, with maximum differences up to $\Delta Cp_{fluct\text{-}max.}$ ~ −23% (see Fig. 14a), for λ_{fs} = 7.82 m^{-1},T_{2L} and $\Delta Cp_{fluct\text{-}max.}$ ~ −25% for λ_{fs} = 1.56 m^{-1},T_L. Similarly to the effect on the side wall (Fig. 12a), the presence of windward façade greening changes the separation behaviour from the roof's upstream edge and introduces a damping effect (Fig. 14a), which is also noticeable in the mean value (ΔCp_{mean} ≤−19%) (Fig. 13a). Again, the effect of both vegetation layers is similar.

Comparing the cases of a thick, low permeability with a thin, high permeability vegetation layer, the most prominent effect seems to be from the façade greening on the fluctuating pressure coefficient. Although rooftop greening has induced changes in the mean pressure on the upstream face and shown a significant damping of pressure fluctuations on the roof (Fig. 14b), these effects are far from the openings and will not affect the air exchange through them.

Façade and rooftop greening effects on the external surface pressure distribution of a model building are not readily available in the literature, for comparison. However, one could assume that the effects would be analogous to those of a double-skin porous façade system (DSF),

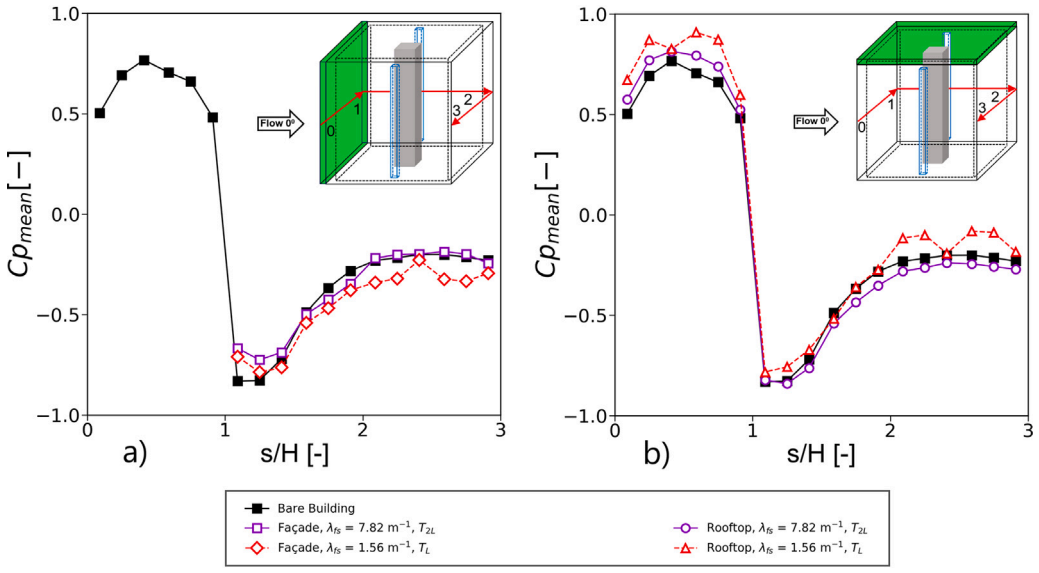

Fig. 11. Mean pressure coefficients, Cp_{mean} of bare building in comparison with (a) façade greening and (b) rooftop greening configurations, of two greening pressure loss coefficients, along the horizontal line, at mid-height.

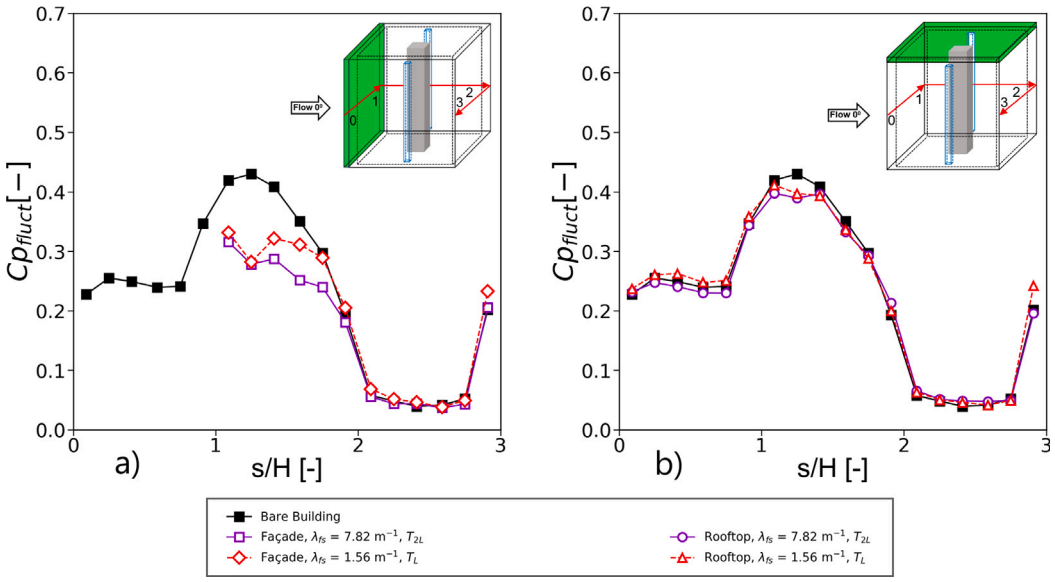

Fig. 12. Fluctuating pressure coefficients Cp_{fluct} of bare building in comparison with (a) façade greening and (b) rooftop greening configurations, of two greening pressure loss coefficients, along the horizontal line, at mid-height.

which is also a layer of porous material installed on the external surface of the building. Hu et al. (2017) recently performed a wind tunnel study of a building with a double-skin façade (DSF) installed at a distance (gap) from the windward wall. The DSF had vertical openings that could provide different levels of porosity. Their measurements show that the pressure fluctuations on the side walls are much smaller in the presence of these vertical openings. They attributed this finding to the jet flow exiting the gap between the windward wall and the façade, at the sidewall leading edge. The jet forms a virtual barrier between the shear layer separating from the leading edge and the side wall. As a result, the interaction between the shear layer and the side wall is less intense and the flow fluctuations near the wall are attenuated. Pomaranzi et al. (2020), also focused on the pressure distribution in the presence of a double-skin porous façade system (DSF) and in particular on the internal glazed façade when an external porous mesh is installed. It was found that the absolute mean values and standard deviations of the pressure signals are generally lower when the porous DSF system is present. Such a filtering effect of the mesh is particularly evident in the suction regions at the strongest wind direction, where the standard deviation of the recorded pressures were halved. These findings are consistent with the subdued pressure fluctuations that have been observed here, under the influence of vegetation layers directly installed on the building's windward wall and rooftop.

4.5. Effects of greening properties

We now proceed to examine the effect of a more systematic variation of façade greening properties. A path is defined, transverse to the streamwise direction, beginning from the middle of the side wall's bottom edge and then continuing across the roof (see Fig. 15). A total of seven different types of greening layers are installed on the windward façade, four thick layers (Fig. 15a) and three thinner ones (Fig. 15b). Based on the observation in Section 4.4 that the major effect of interest

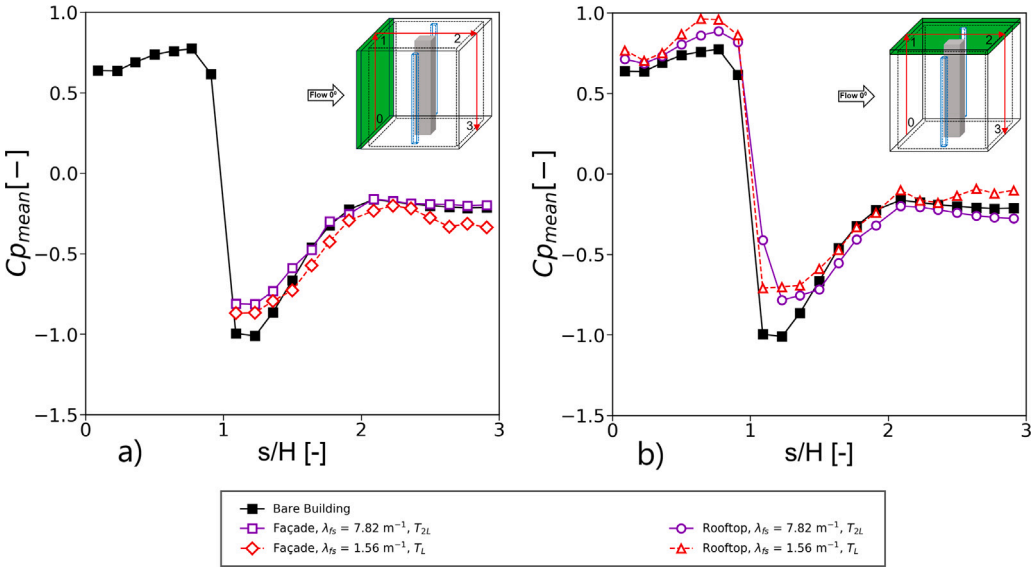

Fig. 13. Mean pressure coefficients, Cp_{mean} of bare building in comparison with (a) façade greening and (b) rooftop greening configurations, of two greening pressure loss coefficients, along the central vertical line.

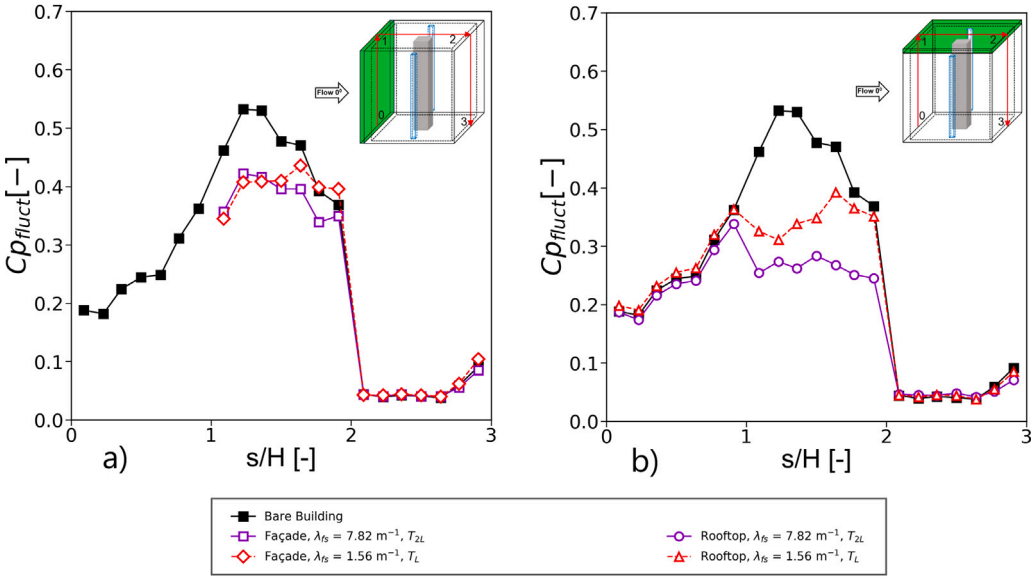

Fig. 14. Fluctuating pressure coefficients Cp_{fluct} of bare building in comparison with (a) façade greening and (b) rooftop greening configurations, of two greening pressure loss coefficients, along the central vertical line.

is on the pressure fluctuations, Cp_{fluct}, we first focus on them along the chosen path, and in the vicinity of the openings.

When a thick layer of greening is installed on the windward face, the lower the pressure loss coefficient, the higher the damping of the fluctuations on the side wall (Fig. 15a), reaching a maximum reduction of $\Delta Cp_{fluct\text{-}max.}$ = 27–44% between the two extreme cases. Additionally, the response on the roof also seems to be sensitive to the pressure loss coefficient values with the lower value of λ_{fs} = 0.83 m^{-1},T_{2L} causing the most damping (~29%). For the thinner greening layer (T_L, see Fig. 15b) the effects are not as clear, particularly for the roof, and the damping of the side wall fluctuations is less (≤21%) compared to the case of the thicker greening layers (Fig. 15a). For the most permeable of the three thin layers examined, λ_{fs} = 0.65 m^{-1},T_L the damping effect is minimal (≤2%) as it is most likely below a threshold that makes any significant difference to the flow.

These results point to the combined effect of the thickness and permeability of the greening layer. According to Eq. (2), the pressure loss is dependent on the value of the product $\lambda{\cdot}T$ and with the values in Table 1, one would expect the layer with λ_{fs} = 0.83 m^{-1},T_{2L} to induce nearly the same pressure loss as the layer with λ_{fs} = 1.56 m^{-1},T_L since their $\lambda{\cdot}T$ values differ by less than 10%. The same is true for the pair of layers with λ_{fs} = 3.04 m^{-1},T_L and λ_{fs} = 1.67 m^{-1},T_{2L}. However, the $\lambda{\cdot}T$ values among layers with the same thickness differ by a factor of two (see Table 1). One may consider an issue with the low velocities that appear near the solid surface and pass through the greening layers as they may belong to a Darcy (linear) regime instead of the quadratic Forchheimer dependence found from the current measurements (see Fig. 4). However, the λ values in the Darcy regime will be larger for all layers and the difference more pronounced, if at all, for the denser ones (Dukhan and Minjeur, 2011). This will lead to an even larger (than twofold) difference in $\lambda{\cdot}T$ for layers of the same thickness, which is still significantly higher than any increase in the 10% differences defined above in the layer pairs of the "same" $\lambda{\cdot}T$.

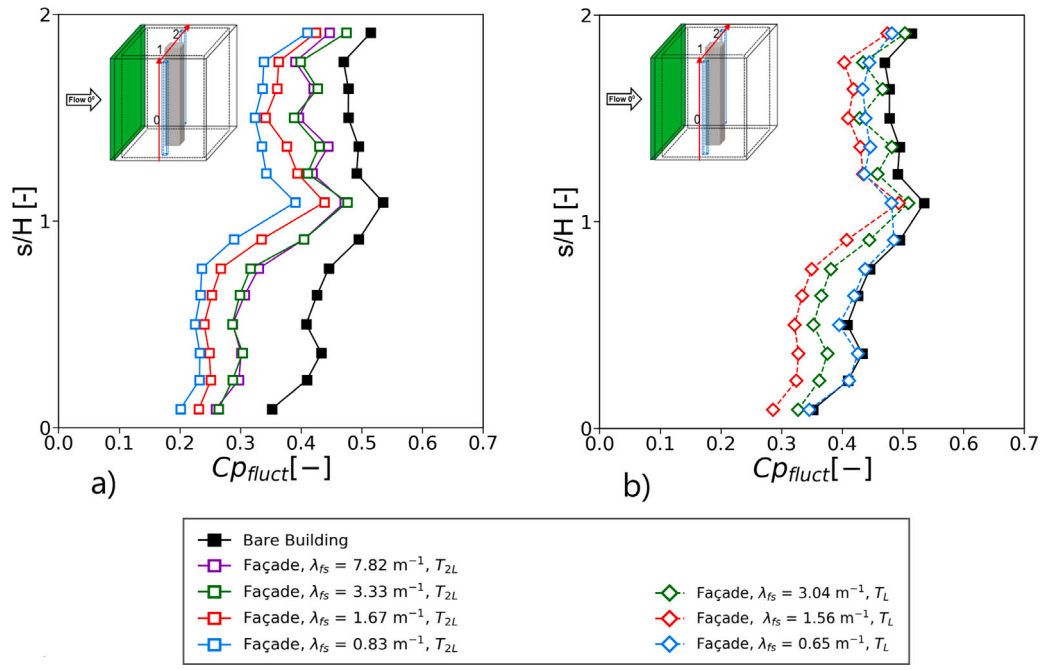

Fig. 15. Fluctuating pressure coefficients Cp_{fluct} of bare building (black) in comparison with façade greening configuration, of (a) four thicker greening pressure loss coefficients,T_{2L} and of (b) three thinner greening pressure loss coefficients,T_L, before right wall lateral opening.

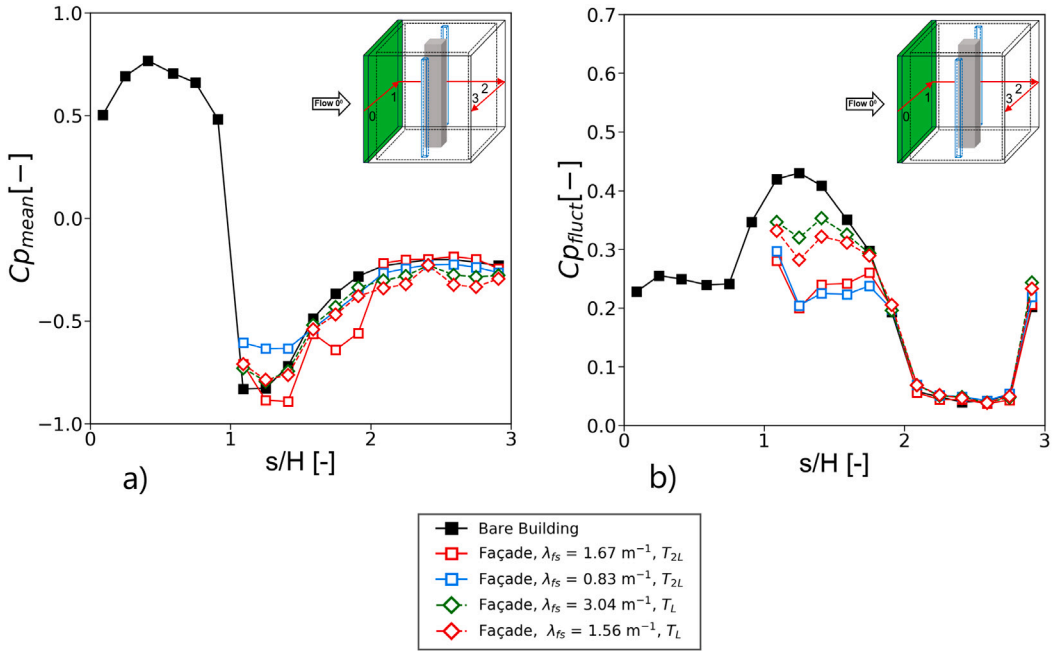

Fig. 16. (a) Mean pressure coefficients, Cp_{mean} and (b) fluctuating pressure coefficients, Cp_{fluct} of bare building in comparison with façade greening, of four greening pressure loss coefficients, along the horizontal line, at mid-height.

We return to examine the mean pressure distributions to investigate the effect of these greening layer pairs i.e. pairs with the "same" $\lambda{\cdot}T$ in Figs. 16a and 17a along the horizontal and vertical paths already defined in previous figures. It is interesting to note that for both the horizontal (Fig. 16a) and the vertical (Fig. 17a) paths, the effect of the thin vegetation layers on the mean pressure distribution is quite similar, in spite of the fact that their $\lambda{\cdot}T$ values differ by a factor of two. For the thicker greening layers, there are discernible differences in the pressure distribution, both on the roof (Fig. 17a) and on the side wall (Fig. 16a), where separation is expected. In Figs. 16b and 17b the effects on the fluctuating pressure coefficient are presented, along the same paths as in Fig. 12 and Fig. 14. The effects are much clearer here. The thickness of the greening layer is what determines the damping of the fluctuations on both the side wall and the roof, with the thicker layers providing more damping (~37%). The effect of pressure loss coefficient for layers of the same thickness is minor even though the difference in their induced pressure drop is twofold.

It seems that interpretation of the results should not be based on the pressure loss alone but these should be based on the product of thickness and pressure loss coefficient ($\lambda{\cdot}T$), given the same flow velocity. When a fluid enters a porous medium, entrance effects will lead to an increased pressure drop for the first part of the flow path

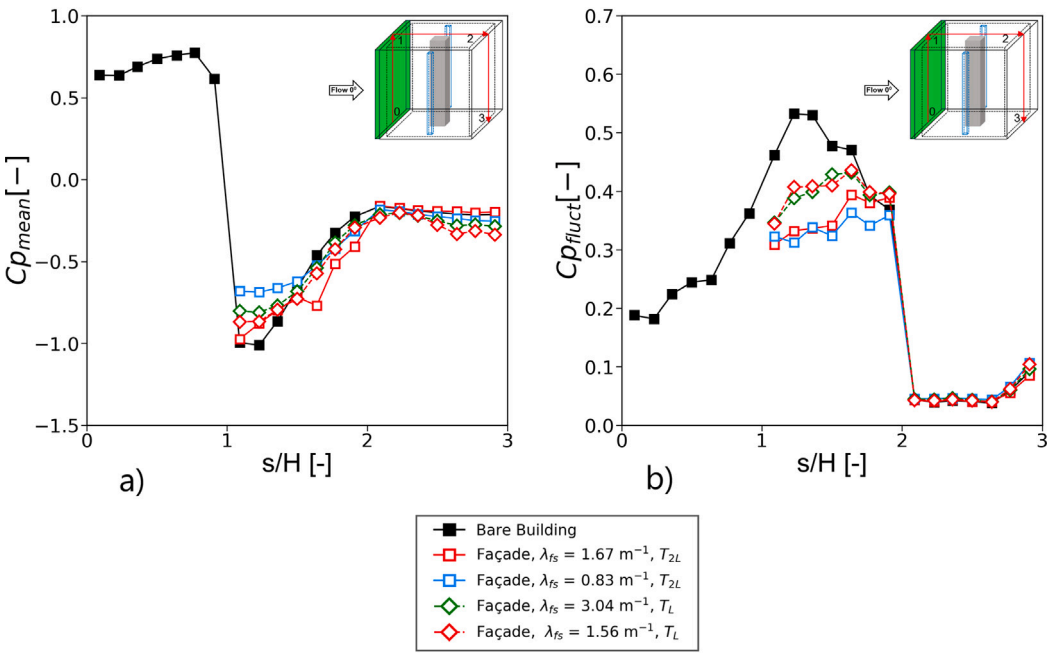

Fig. 17. (a) Mean pressure coefficients, Cp_{mean} and (b) fluctuating pressure coefficients, Cp_{fluct} of bare building in comparison with façade greening, of four greening pressure loss coefficients, along the central vertical line.

and then, when a fully developed regime is established, a lower but constant, pressure drop sets in Kopanidis et al. (2010) and Dukhan and Patel (2011). This effect will obviously be more pronounced, the thinner the porous medium in the direction of the flow. However, in the present case where the flow has a "choice" of either passing through the porous layer or bypassing it, we posit that thin greening layers with a low pressure loss coefficient will allow a significant part of the flow to pass through the layer. On the other hand, thick layers with high pressure loss coefficient will favour a bypass of a large part of the flow. The lower the pressure loss coefficient (high permeability), the more flow through the greening (less bypass) can be expected. The thickness of the greening layer will affect the position of this pressure loss with respect to the solid surface, thus playing an important role in determining the flow that comes into contact with the surface downstream, and also influencing the separation that occurs and the pressure distribution beneath it. The major effect is in the interaction between the flow through the greening layer and the flow structures on the building surfaces. The greening layer thickness is altering the geometry of the building while simultaneously altering the flow. This could be behind the observations in Figs. 16b and 17b, where greening layers of the same thickness behave in the same manner for the fluctuating pressures, regardless of the pressure loss they are expected to induce for the same flow velocity. However, due to the above mentioned effect, it is possible that the mean flow velocity also is different for greening layers of different thickness. This may also explain why the mean pressure distribution changes with pressure loss coefficient for the thick layers but not for the thin ones (Figs. 16a and 17a), whose size is not sufficient to significantly alter the flow.

In terms of pressure fluctuations, the damping effect in thick greening layers is expected to be more obvious for higher permeabilities, as they will be damping a larger proportion of the flow fluctuations (Fig. 15a compared to Fig. 15b). These higher permeability layers will also be subject to the entrance effects mentioned above as the open cell porous material used to represent the greening will include only a limited number of pore cells in the layer. However, as the permeability is reduced, bypass of the flow is induced and there is less flow passing through the greening layer (Fig. 15a) compared to high permeabilities, where damping may not depend as much on the value of the pressure loss coefficient. It is clear that neither the pressure drop alone nor the greening properties (pressure loss coefficient, thickness) are sufficient to explain the effects on the pressure distribution. It appears that the flow bypassing or passing through the vegetation layer is determined by both the thickness of the layer and the pressure loss coefficient. Further information from flow properties such as velocities in the vicinity of the greening layer is obviously necessary. Thus, velocity measurements at the openings and around the model building (side wall, roof, wake) are in progress in order to enlighten and/or reinforce our assumptions about the flow-field near the green-plant layer and correlate them with the pressure and tracer gas measurements.

4.6. Power spectrum analysis

The effects of greening on the mean pressure distribution of the external surfaces are discernible but the major effect of interest to the air exchange through the openings was found on the standard deviation i.e. the pressure fluctuations. A further step to analyse this finding was made through a frequency analysis. The non-dimensional power spectral density has been calculated for a meaningful frequency range at the wind tunnel scale, as shown in Figs. 18–20. It was found that the energy content in the pressure fluctuation dropped by at least one order of magnitude for frequencies above 60 Hz and so the range f = 0–60 Hz is presented with a resolution of 0.33 Hz, while a zoom-in for frequencies below 5 Hz is also included in the Figs. 18–20, for panels (a)–(f), which were found sufficient to show the variations and the effects. In Fig. 18, spectra are shown for four of the thick façade greening layers and are compared with that of the bare building at six measurement taps at mid-height along the side wall. Fig. 19 presents the spectra for three thin greening layers at the same six measurement taps. This permits evaluation of the behaviour from the leading edge, across the opening and up to the downstream edge.

It is evident from all the graphs in Fig. 18 and in Fig. 19 that the effect of façade greening extends through the whole range of frequencies presented but the major effect is in the lower frequency range (0–30 Hz). The differences are less evident downstream and after the opening, becoming almost negligible towards the downstream vertical edge (Figs. 18e–f and 19e–f). Upstream and near the opening is also the region where the mean and fluctuating pressure coefficients exhibit a significant drop (Figs. 11a and 12a, respectively) and these

high gradients are also present in the bare building case. It is difficult to tell, without input from velocity measurements, if this is the edge of the recirculation zone or if it is the opening that causes the steep streamwise gradient in mean and fluctuating pressure. However, the effect of greening is clear: it is the lower frequencies that are mostly damped immediately downstream of the leading edge and it is the lower pressure loss coefficient layers that cause the most damping (Fig. 18).

It is interesting to note that the sensitivity of the damping to the layers' pressure loss coefficient is mainly evident at frequencies below 30 Hz (Fig. 18a–d). At higher frequencies and downstream positions (Fig. 18d-e) damping does not show any significant sensitivity to the vegetation properties i.e. all vegetation layers behave almost the same.

The thin greening layers in Fig. 19 show a slightly different behaviour with the highly permeable greening having hardly any effect and the two denser greening layers behaving in almost exactly the same manner, in accordance with the observations of Fig. 15b. The damping caused by these two layers in Fig. 19a-d is similar (~33% between f = 0–30 Hz) to that of the denser and thicker layer (λ_{fs} = 7.82 m^{-1},T$_{2L}$) in Fig. 18a-d. This is also in agreement with the behaviour of the façade greening layers shown in Figs. 11–14 where reduced fluctuation pressure coefficients were found at these positions.

Taking into account the greening layer pairs with the same $\lambda{\cdot}T$ values as mentioned before: (λ_{fs} = 0.83 m^{-1},T$_{2L}$ with λ_{fs} = 1.56 m^{-1},T$_L$) and (λ_{fs} = 3.04 m^{-1},T$_L$ with λ_{fs} = 1.67 m^{-1},T$_{2L}$), Fig. 20 shows a prominent effect of greening thickness. The layers belonging to each pair of similar $\lambda{\cdot}T$ do not have the same damping behaviour. However, layers of common thickness do behave similarly with the thicker layers damping out more than half of the energy content near the leading edge (Fig. 20a–b) and by far exceeding the damping of the thinner ones up to halfway downstream (Fig. 20c–d). The difference between the two thicknesses is not distinguishable above 50 Hz or near the downstream edge (Fig. 20e–f).

One would obviously expect a flow passing through a porous medium to be subject to an effect on its frequency content. However, in the present case, the fact that the porous medium (vegetation) is attached to a bluff body (building) creates an interaction with the flow that is not present in the case where the flow is forced to pass through this porous medium e.g. when measuring the pressure loss coefficient. The bypass mechanism discussed above and the variation of the frequency content with the material properties of the vegetation are shown here for the first time.

Haghighat et al. (1991) were among the first to analyse fluctuating air change rates and Xiao et al. (2022) recently presented a comprehensive review of modelling approaches to natural ventilation due to wind fluctuations. They refer to the widely accepted types of turbulent ventilation mechanisms as continuous airflow, pulsating flow and eddy penetration. These have recently been supplemented by pumping ventilation, which refers to a specific type of pulsating flow at a leeward building opening. It is important to discern these mechanisms with respect to the frequency range and the direction of the flow. According to Straw et al. (2000), the continuous flow mechanism can be considered as broad-band in the sense that it appears as the result of surface pressure fluctuations across a wide range of frequencies. The pulsating flow mechanism is a result of fluid flow parallel to the plane of an opening, resulting from pressure differences between the inner and outer sides of the opening. It is dependent on the geometry of the opening and the compressibility of the fluid and will have a frequency peak at the Helmholtz resonant frequency of the enclosure. Eddy penetration refers to fluid entering the enclosure due to the unstable behaviour of shear layers or vortex shedding that passes over the opening. Ai and Mak (2014) performed LES simulations of the flow past a cube with a single opening and found that when this occurs on the side wall (parallel to the flow) the contribution of turbulent flow to the total air exchange is over 63%, as opposed to only 14% for a windward opening.

The work of Straw et al. (2000) is highly relevant to the present work as it involves full scale measurements of pressure fluctuations on a 6 m cubic structure exposed to turbulent flow with two openings on its side walls (parallel to the flow). They found that the effect of the pulsating flow mechanism (relevant to resonance) was an order of magnitude less than the broad band and eddy penetration mechanisms. The resonant/natural frequency of an enclosure (ω_n) can be estimated as (Straw et al., 2000):

$$\omega_n = \left(\frac{ABN}{\rho L}\right)^{0.5} \tag{9}$$

$$B = \frac{\gamma PR}{V} \tag{10}$$

where ρ is the density of air, A is the area of the opening, L is the effective orifice length (actual orifice length $+0.89\sqrt{A}$), N is the number of orifices, γ is the ratio of specific heats, PR is a reference pressure and V is the volume of the enclosure.

For the present case, one finds $f_n = \omega_n/2\pi \sim 353$ Hz. From Figs. 18–20, the fluctuation frequencies being measured at the side wall are much lower and this is an indication that the main mechanism will most probably not belong to any high frequency Helmholtz regime but rather the broadband (i.e. continuous flow) and/or the eddy penetration mechanism i.e. unsteadiness of the recirculation zone on the side walls.

The fact that greening affects only the lowest frequency range (Figs. 18–20), supports the fact that its presence is affecting the large scale structures of the flow around the building. These structures are expected to be affected by the mechanism proposed earlier in this study that the vegetation layer thickness and the permeability are damping the portion of the flow that does not bypass the layer and thus the separation and unsteadiness of the flow is modified. Both of these are expected to be major mechanisms for air exchange through openings on the building side walls.

5. Summary and conclusions

In this study, the aerodynamic effects of façade and rooftop greening were investigated on a simplified model building exposed to an urban atmospheric boundary layer. The model building has a cubic geometry and two openings on its side walls, namely those parallel to the incoming flow. A porous foam medium with different pressure loss coefficients λ, thicknesses T and porosities ϵ, was used to model different types of greening and greening species. During the experimental procedure, the same scale factor M = 1:300 was used for the atmospheric boundary layer, the model building, its openings, and the greening. Time-resolved surface pressure measurements were performed on the outer surfaces of the model building.

A general outcome of this study is that the greening position has a major effect on the pressure distribution. In particular, it is deduced that both rooftop and windward façade greening have a major influence, not only on the mean, but mostly on the fluctuating pressure distribution. Rooftop greening reduces the magnitude of the rooftop suction pressure and increases the upstream face stagnation pressure by ~30%, compared to the building without vegetation. The windward façade greening has a similar effect on the side wall adjacent to the opening, where the damping of the fluctuating pressure signal can be ~35% in comparison to the bare building.

The two kinds of greening, namely façade and rooftop greening, were also tested for four different permeabilities expressed by the pressure loss coefficient at two thicknesses. It seems that the effect of greening layer thickness is more pronounced for façade greening than for rooftop greening. With a thick greening layer on the windward façade, the higher the permeability, the greater the damping of pressure fluctuations on the side wall where the opening is located. It is presumed that the lower pressure loss coefficient permits more flow through the greening layer, rather than diverting it around it (bypass

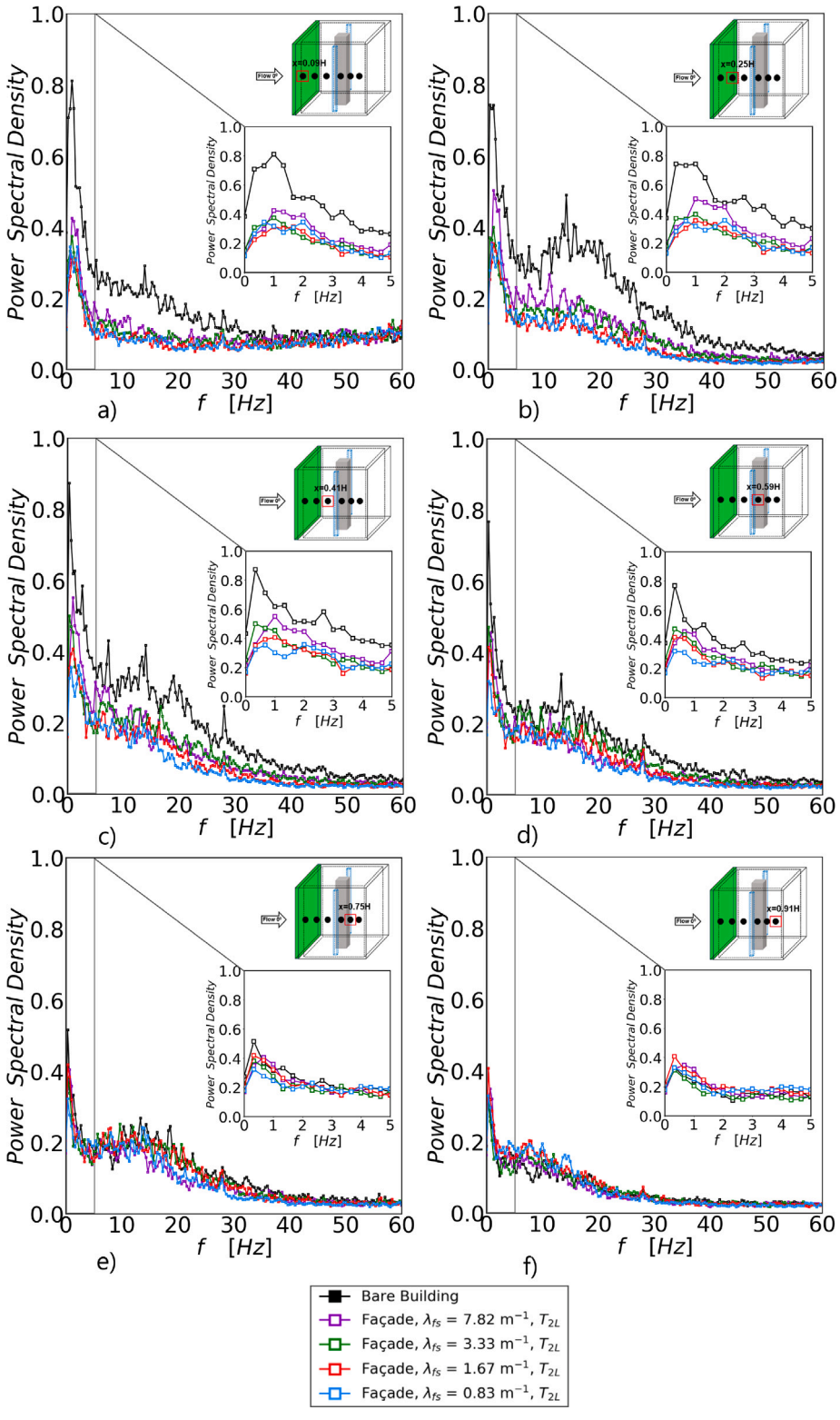

Fig. 18. Power spectrum density of instantaneous pressure signal for façade greening configuration, of four thicker pressure loss coefficients, at six different left wall taps positioning, at mid-building height: (a) x = 0.09H (leading edge), (b) x = 0.25H, (c) x = 0.41H (before side opening), (d) x = 0.59H (after side opening), (e) x = 0.75H and (f) x = 0.91H (trailing edge).

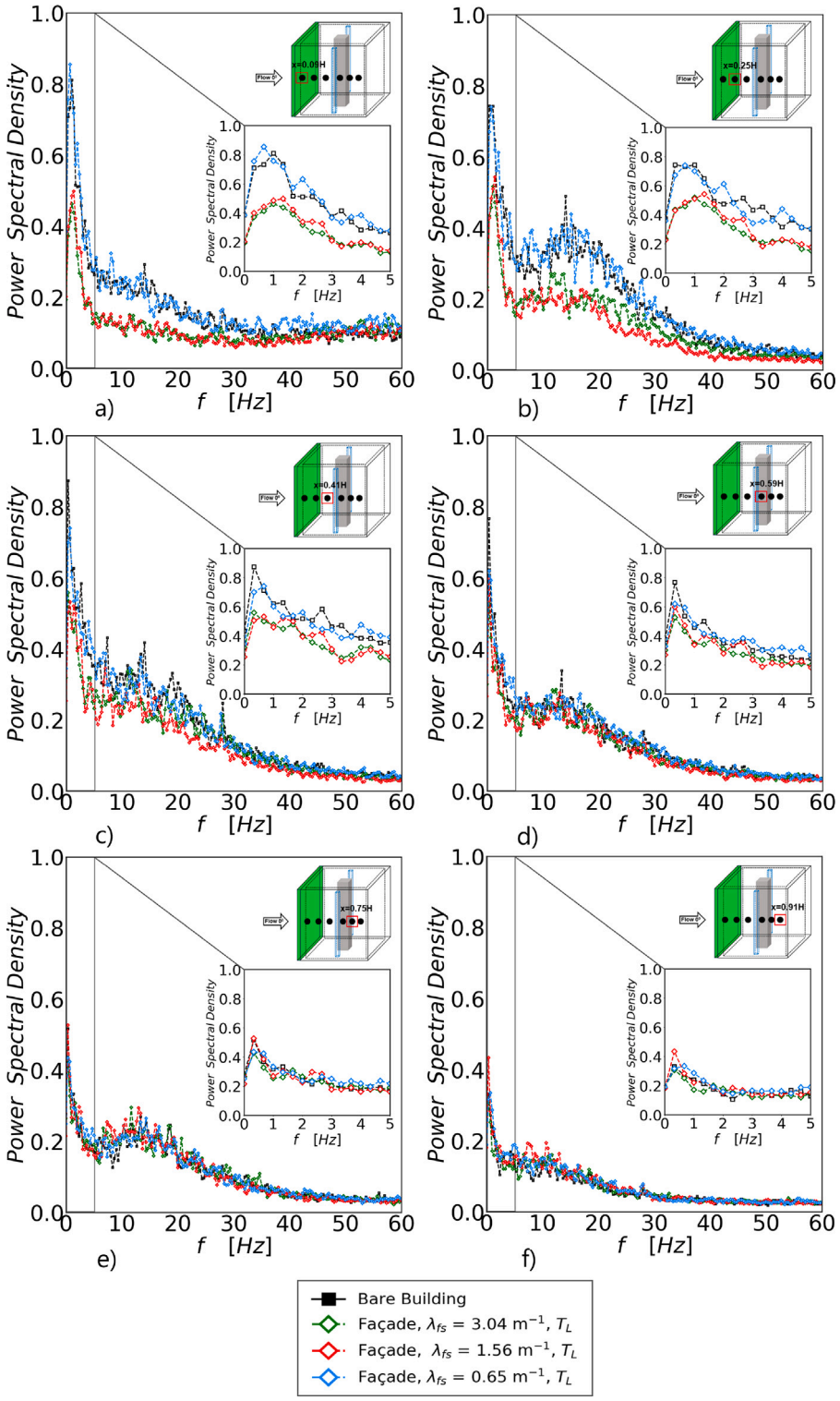

Fig. 19. Power spectrum density of instantaneous pressure signal for façade greening configuration, of three thinner pressure loss coefficients, at six different left wall taps positioning, at mid-building height: (a) x = 0.09H (leading edge), (b) x = 0.25H, (c) x = 0.41H (before side opening), (d) x = 0.59H (after side opening), (e) x = 0.75H and (f) x = 0.91H (trailing edge).

effect). This leads to reductions of the suction pressures range between 24% and 41% compared to the reference case. A thinner greening layer with low pressure coefficient has hardly any effect on the flow but if the resistance of the thin layer increases, damping occurs, although lower than for the thick layer, with maximum relative differences of ~22%.

Another interesting finding of the present study is the influence of façade greening on the power spectral density. The frequency analysis of the side wall measurement points at mid-building height reveals that it is the lower frequencies, i.e. below 50 Hz, that are mainly influenced by the presence of windward façade greening. However, the effect of the greening's permeability is more pronounced at frequencies below 30 Hz. It is also concluded that the thicker greening layers with lower pressure loss coefficients (higher permeability) cause the greatest damping of the power spectrum. On the contrary, the thinner façade

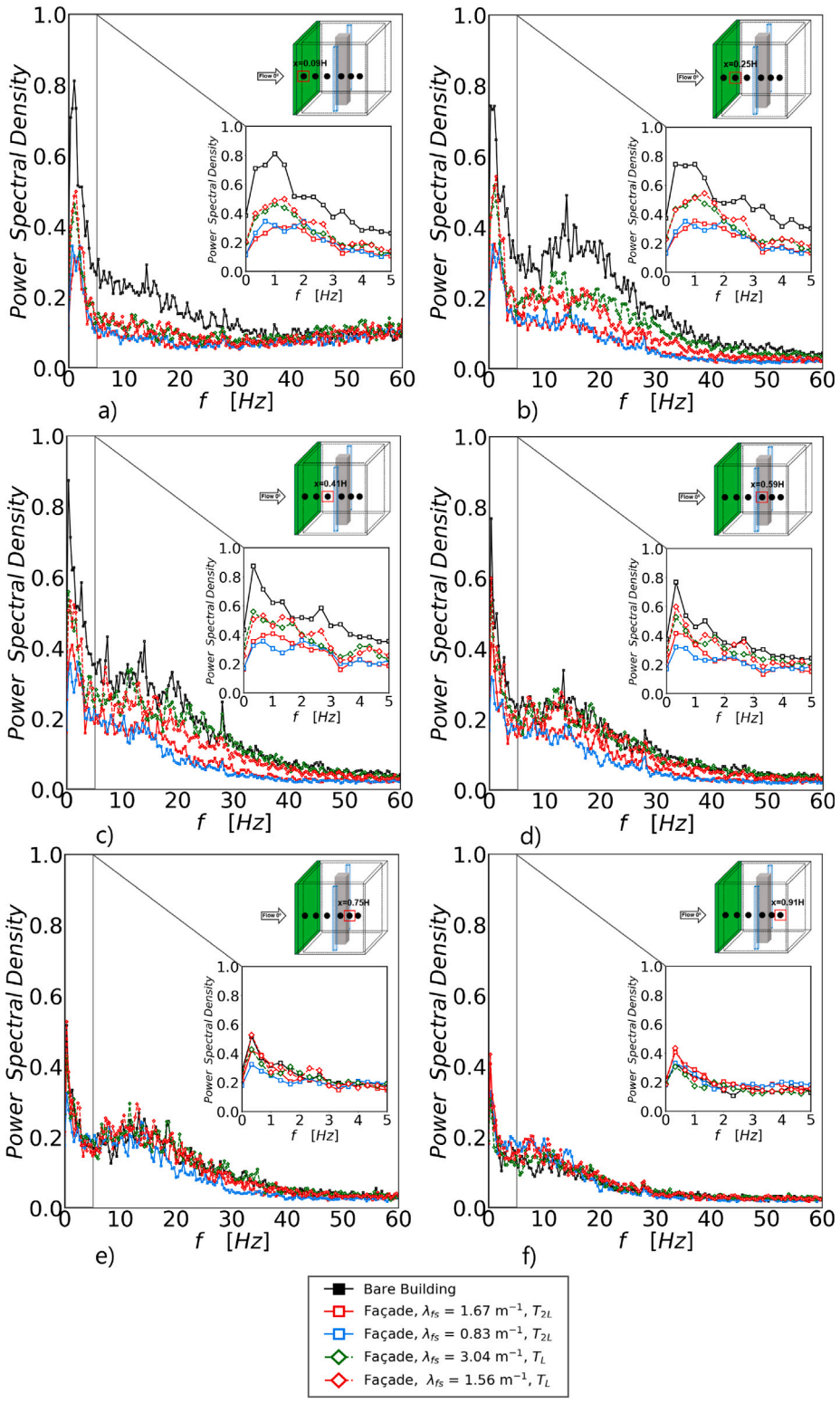

Fig. 20. Power spectrum density of instantaneous pressure signal for façade greening configuration, of four thick and thin pressure loss coefficients, at six different left wall taps positioning, at mid-building height: (a) x = 0.09H (leading edge), (b) x = 0.25H, (c) x = 0.41H (before side opening), (d) x = 0.59H (after side opening), (e) x = 0.75H and (f) x = 0.91H (trailing edge).

greening layers with high permeability expressed by the pressure loss coefficient, induce almost no effect, which leads to similar results as with a bare building. This behaviour may also be attributed to the bypass effect observed in the pressure measurements.

Finally, it should be noted that although the similarity criterion for modelling vegetation in reduced scale experiments assumes that, for the same dynamic pressure, the pressure loss, i.e. the product of thickness and pressure loss coefficient, should be the same at the model scale and at full scale, the results of the pressure measurements point to the conclusion that the thickness and/or the pressure loss coefficient follow the same principle as an independent parameter. It is clear, however, that neither the pressure drop alone, nor the greening properties (pressure loss coefficient, thickness) are enough to explain the effects on the pressure distribution. It seems that the flow bypassing or passing through the greening layer is determined by both the layer's thickness and the pressure loss coefficient. This, in turn, is reflected upon the pressure distribution and the damping of the lower frequencies of the pressure fluctuations and is expected to carry over to other dependent parameters such as air exchange through openings.

In summary, this is the first wind tunnel study to investigate the effects of windward façade greening and rooftop greening on the pressure distribution of a scale model building. The results complement an earlier study in which the influence of the greening position on the air exchange rate was investigated (Pappa et al., 2023). Although multiple wind directions and sheltered building conditions were not tested, the future availability of flow field measurements will provide an holistic picture and the role of building embedded vegetation will become clearer under these specific measurement conditions.

CRediT authorship contribution statement

Vasiliki Pappa: Validation, Formal analysis, Writing – original draft, Methodology, Visualization, Funding acquisition, Writing – review & editing, Software, Conceptualization. **Asterios Bakolas:** Formal analysis, Resources, Investigation. **Demetri Bouris:** Supervision, Funding acquisition, Writing – review & editing, Project administration, Writing – original draft, Methodology, Resources, Conceptualization. **Christof Gromke:** Writing – review & editing, Investigation, Resources, Methodology, Supervision, Conceptualization.

Declaration of competing interest

The authors declare that they have no known competing financial interests or personal relationships that could have appeared to influence the work reported in this paper.

Acknowledgements

This work was financially supported by the European Union's Horizon research and innovation programme TWEET-IE (Grant Agreement Number: 101079125, Call Topic: HORIZON-WIDERA-2021-ACCESS-03-01). The first author also gratefully acknowledges support from a scholarship from NTUA Research Committee (grant: 65219100). Furthermore, the authors are grateful to Armin Reinsch for his support during the wind tunnel experiments. The publication of the article in OA mode was financially supported by HEAL-Link.

Data availability

Data will be made available on request.

References

Ai, Z.T., Mak, C.M., 2014. Analysis of fluctuating characteristics of wind-induced airflow through a single opening using LES modeling and the tracer gas technique. Build. Environ. 80, 249–258. http://dx.doi.org/10.1016/J.BUILDENV.2014.06.002.

Aldheeb, M., Asrar, W., Sulaeman, E., Omar, A.A., 2018. Aerodynamics of porous airfoils and wings. Acta Mech. 229 (9), 3915–3933. http://dx.doi.org/10.1007/s00707-018-2203-6.

Antohe, B.V., Lage, J.L., Price, D.C., Weber, R.M., 1997. Experimental determination of permeability and inertia coefficients of mechanically compressed aluminum porous matrices. J. Fluids Eng. Trans. ASME 119 (2), 404–412, URL https://doi.org/10.1115/1.2819148.

Aubrun, S., Leitl, B., 2004. Development of an improved physical modelling of a forest area in a wind tunnel. Atmos. Environ. 38 (18), 2797–2801. http://dx.doi.org/10.1016/j.atmosenv.2004.02.035.

Bekkers, C.C., Angelou, N., Dellwik, E., 2022. Drag coefficient and frontal area of a solitary mature tree. J. Wind Eng. Ind. Aerodyn. 220, http://dx.doi.org/10.1016/j.jweia.2021.104854.

Bergh, H., Tijdeman, H., 1965. Theoretical and Experimental Results for the Dynamic Response of Pressure Measuring Systems. Tech. Rep., National Lucht- en Ruimtevaartlaboratorium (NL), p. 51.

Besir, A.B., Cuce, E., 2018. Green roofs and facades: A comprehensive review. http://dx.doi.org/10.1016/j.rser.2017.09.106.

Biswas, S., Vanderwel, C., 2024. Flow through a hollow cube in a turbulent boundary layer: towards understanding indoor pollutant dispersion. Flow 4, http://dx.doi.org/10.1017/flo.2024.14.

Boomsma, K., Poulikakos, D., 2002. The effects of compression and pore size variations on the liquid flow characteristics in metal foams. J. Fluids Eng. Trans. ASME 124 (1), 263–272. http://dx.doi.org/10.1115/1.1429637.

Buccolieri, R., Santiago, J.L., Rivas, E., Sanchez, B., 2018. Review on urban tree modeling in CFD simulations: Aerodynamic, deposition and thermal effects. Urban For. Urban Green. 31, 212–220. http://dx.doi.org/10.1016/j.ufug.2018.03.003.

Cao, J., Tamura, Y., Yoshida, A., 2012. Wind tunnel study on aerodynamic characteristics of shrubby specimens of three tree species. Urban For. Urban Green. 11 (4), 465–476. http://dx.doi.org/10.1016/j.ufug.2012.05.003.

Cao, Y., Tamura, T., Zhou, D., Bao, Y., Han, Z., 2022. Topological description of near-wall flows around a surface-mounted square cylinder at high Reynolds numbers. J. Fluid Mech. 933, http://dx.doi.org/10.1017/jfm.2021.1043.

Castro, I., Robins, A., 1977. The flow around a surface-mounted cube in uniform and turbulent streams. J. Fluid Mech. 79 (2), 307–335.

Chu, C.R., Chen, R.H., Chen, J.W., 2011. A laboratory experiment of shear-induced natural ventilation. Energy Build. 43 (10), 2631–2637. http://dx.doi.org/10.1016/j.enbuild.2011.06.014.

Ciarlatani, M.F., Huang, Z., Philips, D., Gorlé, C., 2023. Investigation of peak wind loading on a high-rise building in the atmospheric boundary layer using large-eddy simulations. J. Wind Eng. Ind. Aerodyn. 236, http://dx.doi.org/10.1016/j.jweia.2023.105408.

Cook, N., 1978. Wind-tunnel simulation of the adiabatic atmospheric boundary layer by roughness, barrier, and mixing-device methods. J. Ind. Aerodyn. 3, 157–176.

Dellwik, E., Romanic, D., Mann, J., Enuş, M., Hangan, H., 2023. Forest edge representation in scaled experiments: A flexible approach for matching to field observations. Bound.-Layer Meteorol. 187 (3), 793–817. http://dx.doi.org/10.1007/s10546-023-00796-z.

Dukhan, N., Minjeur, C., 2011. A two-permeability approach for assessing flow properties in metal foam. J. Porous Mater. 18 (4), 417–424. http://dx.doi.org/10.1007/s10934-010-9393-1.

Dukhan, N., Patel, K., 2011. Effect of sample's length on flow properties of open-cell metal foam and pressure-drop correlations. J. Porous Mater. 18 (6), 655–665. http://dx.doi.org/10.1007/s10934-010-9423-z.

Etheridge, D., Sandberg, M., 1996. Building Ventilation Theory and Measurement. John Wiley & Sons, Chichester.

Eurocode, 2005. Actions on structures - Part 1- 4: General actions - Wind actions. 1991. In: Authority: The European Union Per Regulation 305/2011, Directive 98/34/EC, Directive 2004/18/EC.

European Environment Agency, 2024. (EEA). URL https://www.eea.europa.eu/en/analysis/maps-and-charts/mean-wind-speed.

Fellini, S., Marro, M., Del Ponte, A.V., Barulli, M., Soulhac, L., Ridolfi, L., Salizzoni, P., 2022. High resolution wind-tunnel investigation about the effect of street trees on pollutant concentration and street canyon ventilation. Build. Environ. 226, http://dx.doi.org/10.1016/j.buildenv.2022.109763.

Gosselin, F.P., 2019. Mechanics of a plant in fluid flow. J. Exp. Bot. 70 (14), 3533–3548. http://dx.doi.org/10.1093/jxb/erz288.

Gromke, C., 2011. A vegetation modeling concept for building and environmental aerodynamics wind tunnel tests and its application in pollutant dispersion studies. Environ. Pollut. 159 (8–9), 2094–2099. http://dx.doi.org/10.1016/j.envpol.2010.11.012.

Gromke, C., 2018. Wind tunnel model of the forest and its Reynolds number sensitivity. J. Wind Eng. Ind. Aerodyn. 175, 53–64. http://dx.doi.org/10.1016/j.jweia.2018.01.036.

Gromke, C., Jamarkattel, N., Ruck, B., 2016. Influence of roadside hedgerows on air quality in urban street canyons. Atmos. Environ. 139, 75–86. http://dx.doi.org/10.1016/j.atmosenv.2016.05.014.

Gromke, C., Ruck, B., 2012. Pollutant concentrations in street canyons of different aspect ratio with avenues of trees for various wind directions. Bound.-Layer Meteorol. 144 (1), 41–64. http://dx.doi.org/10.1007/s10546-012-9703-z.

Grunert, F., Benndorf, D., Klingbeil, K., 1984. Neuere ergebnisse zum aufbau von schutzpflanzungen. Beitrage Forstwirtsch..

Haghighat, F., Brohus, H., Rao, J., 2000. Modelling air infiltration due to wind fluctuations—a review. Build. Environ. 35 (5), 377–385. http://dx.doi.org/10.1016/S0360-1323(99)00028-1.

Haghighat, F., Rao, J., Fazio, P., 1991. The influence of turbulent wind on air change rates - a modelling approach. Build. Environ. 26 (2), 95–109. http://dx.doi.org/10.1016/0360-1323(91)90017-6.

Hayati, A., Mattsson, M., Sandberg, M., 2019. A wind tunnel study of wind-driven airing through open doors. Int. J. Vent. 18 (2), 113–135. http://dx.doi.org/10.1080/14733315.2018.1435027.

Hearst, R.J., Gomit, G., Ganapathisubramani, B., 2016. Effect of turbulence on the wake of a wall-mounted cube. J. Fluid Mech. 804, 513–530. http://dx.doi.org/10.1017/jfm.2016.565.

Holmes, J.D., 1979. Mean and fluctuating internal pressures induced by wind. In: Proceedings of the Fifth International Conference on Wind Engineering. Vol. 1, Pergamon Press, pp. 435–450. http://dx.doi.org/10.1016/b978-1-4832-8367-8.50046-2.

Hu, G., Hassanli, S., Kwok, K.C., Tse, K.T., 2017. Wind-induced responses of a tall building with a double-skin façade system. J. Wind Eng. Ind. Aerodyn. 168, 91–100. http://dx.doi.org/10.1016/j.jweia.2017.05.008.

Ikegaya, N., Hasegawa, S., Hagishima, A., 2019. Time-resolved particle image velocimetry for cross-ventilation flow of generic block sheltered by urban-like block arrays. Build. Environ. 147, 132–145. http://dx.doi.org/10.1016/j.buildenv.2018.10.015.

Jiang, Z., Kobayashi, T., Yamanaka, T., Sandberg, M., Kobayashi, N., Choi, N., Sano, K., 2022. Validity of orifice equation and impact of building parameters on wind-induced natural ventilation rates with minute mean wind pressure difference. Build. Environ. 219, http://dx.doi.org/10.1016/j.buildenv.2022.109248.

Kane, B., Smiley, E.T., 2006. Drag coefficients and crown area estimation of red maple. Can. J. Forest Res. 36 (8), 1951–1958. http://dx.doi.org/10.1139/X06-086.

Karava, P., Stathopoulos, T., Athienitis, A.K., 2011. Airflow assessment in cross-ventilated buildings with operable façade elements. Build. Environ. 46 (1), 266–279. http://dx.doi.org/10.1016/j.buildenv.2010.07.022.

Karoglou, M., Bakolas, A., Moropoulou, A., Papapostolou, A., 2013. Effect of coatings on moisture and salt transfer phenomena of plasters. Constr. Build. Mater. 48, 35–44. http://dx.doi.org/10.1016/j.conbuildmat.2013.06.050.

Klausmann, K., Ruck, B., 2017. Drag reduction of circular cylinders by porous coating on the leeward side. J. Fluid Mech. 813, 382–411. http://dx.doi.org/10.1017/jfm.2016.757.

Kobayashi, T., Sandberg, M., Fujita, T., Lim, E., Umemiya, N., 2022. Numerical analysis of wind-induced natural ventilation for an isolated cubic room with two openings under small mean wind pressure difference. Build. Environ. 226, http://dx.doi.org/10.1016/j.buildenv.2022.109694.

Kopanidis, A., Theodorakakos, A., Gavaises, E., Bouris, D., 2010. 3D numerical simulation of flow and conjugate heat transfer through a pore scale model of high porosity open cell metal foam. Int. J. Heat Mass Transfer 53 (11–12), 2539–2550. http://dx.doi.org/10.1016/j.ijheatmasstransfer.2009.12.067.

Ledda, P.G., Siconolfi, L., Viola, F., Gallaire, F., Camarri, S., 2018. Suppression of von Kármán vortex streets past porous rectangular cylinders. Phys. Rev. Fluids 3 (10), http://dx.doi.org/10.1103/PhysRevFluids.3.103901.

Li, H., Zhao, Y., Sützl, B., Kubilay, A., Carmeliet, J., 2022. Impact of green walls on ventilation and heat removal from street canyons: Coupling of thermal and aerodynamic resistance. Build. Environ. 214, http://dx.doi.org/10.1016/j.buildenv.2022.108945.

Lim, H.C., Castro, I.P., Hoxey, R.P., 2007. Bluff bodies in deep turbulent boundary layers: Reynolds-number issues. J. Fluid Mech. 571, 97–118. http://dx.doi.org/10.1017/S0022112006003223.

Manickathan, L., Defraeye, T., Allegrini, J., Derome, D., Carmeliet, J., 2018. Comparative study of flow field and drag coefficient of model and small natural trees in a wind tunnel. Urban For. Urban Green. 35, 230–239. http://dx.doi.org/10.1016/j.ufug.2018.09.011.

Manolesos, M., Gao, Z., Bouris, D., 2018. Experimental investigation of the atmospheric boundary layer flow past a building model with openings. Build. Environ. 141, 166–181. http://dx.doi.org/10.1016/j.buildenv.2018.05.049.

Mayhead, G., 1973. Some Drag Coefficients for British Forest Trees Derived from Wind Tunnel Studies. Tech. Rep., pp. 123–130.

Papp, B., Kristóf, G., Gromke, C., 2021. Application and assessment of a GPU-based LES method for predicting dynamic wind loads on buildings. J. Wind Eng. Ind. Aerodyn. 217, http://dx.doi.org/10.1016/j.jweia.2021.104739.

Pappa, V., Bouris, D., Theurer, W., Gromke, C., 2023. A wind tunnel study of aerodynamic effects of façade and roof greening on air exchange from a cubic building. Build. Environ. 231, http://dx.doi.org/10.1016/j.buildenv.2023.110023.

Pappa, V., Langidis, A., Manolesos, M., Bouris, D., 2019. Stereo PIV measurements of vertical variation of local ventilation rates for a generic building exposed to an atmospheric boundary layer. In: 11th International Symposium on Turbulence and Shear Flow Phenomena.

Pérez, G., Coma, J., Chàfer, M., Cabeza, L.F., 2022. Seasonal influence of leaf area index (LAI) on the energy performance of a green facade. Build. Environ. 207, 108497. http://dx.doi.org/10.1016/J.BUILDENV.2021.108497.

Pomaranzi, G., Daniotti, N., Schito, P., Rosa, L., Zasso, A., 2020. Experimental assessment of the effects of a porous double skin façade system on cladding loads. J. Wind Eng. Ind. Aerodyn. 196, http://dx.doi.org/10.1016/j.jweia.2019.104019.

Richards, P.J., Hoxey, R.P., 2012. Pressures on a cubic building-Part 1: Full-scale results. J. Wind Eng. Ind. Aerodyn. 102, 72–86. http://dx.doi.org/10.1016/j.jweia.2011.11.004.

Ruck, B., Schmidt, F., 1986. Das strömungsfeld der einzelbaumumströmung. Forstwiss Centralblatt 105, 178–196.

Rudnicki, M., Mitchell, S.J., Novak, M.D., 2004. Wind tunnel measurements of crown streamlining for drag relationships for three conifer species. Can. J. Forest Res. 34 (3), 666–676. http://dx.doi.org/10.1139/x03-233.

Sandberg, M., Kabanshi, A., Wigö, H., 2020. Is building ventilation a process of diluting contaminants or delivering clean air? Indoor Built Environ. 29 (6), 768–774. http://dx.doi.org/10.1177/1420326X19837340.

Seol, C., Kim, T., Kim, T., 2024. The effect of permeability on the flow structure of porous square cylinders. J. Fluid Mech. 985, http://dx.doi.org/10.1017/jfm.2024.311.

Stacey, G.R., Belcher, R.E., Wood, C.J., Gardiner, B., 1994. Wind Flows and Forces in a Model Spruce Forest. Tech. Rep..

Stefano Boeri Architetti, 2014. SBA. URL https://www.stefanoboeriarchitetti.net/en/.

Straw, M.P., Baker, C.J., Robertson, A.P., 2000. Experimental measurements and computations of the wind-induced ventilation of a cubic structure. J. Wind Eng. Ind. Aerodyn. 88 (2–3), 213–230. http://dx.doi.org/10.1016/S0167-6105(00)00050-7.

Tamaro, S., Zamponi, R., Ragni, D., Teruna, C., Schram, C., 2021. Experimental investigation of turbulent coherent structures interacting with a porous airfoil. Exp. Fluids 62 (5), http://dx.doi.org/10.1007/s00348-021-03170-2.

UN Cities, 2015. United nations sustainable development action. URL https://www.un.org/sustainabledevelopment/cities/.

VDI 3783, 2000. Environmental Meteorology Physical Modelling of Flow and Dispersion Processes in the atmospheric boundary layer. Applications of wind tunnels, two thousand ed. Beuth Verlag, Berlin:.

Vollsinger, S., Mitchell, S.J., Byrne, K.E., Novak, M.D., Rudnicki, M., 2005. Wind tunnel measurements of crown streamlining and drag relationships for several hardwood species. Can. J. Forest Res. 35 (5), 1238–1249. http://dx.doi.org/10.1139/x05-051.

Welch, P., 1967. The Use of Fast Fourier Transform for the Estimation of Power Spectra: A Method Based on Time Averaging Over Short. Vol. 15, pp. 70–73. http://dx.doi.org/10.1109/TAU.1967.1161901.

Xiao, X., Zhou, J., Yang, W., 2022. Review of calculating models of unsteady natural ventilation rate due to wind fluctuations. Indoor Built Environ. 31 (9), 2199–2215. http://dx.doi.org/10.1177/1420326X221084033.

Ysebaert, T., Samson, R., Denys, S., 2022. Parameterisation of the drag effect of climbers depending on wind speed and LAD. Sustain. Cities Soc. 84, http://dx.doi.org/10.1016/j.scs.2022.103979.